ChemComm

Design principles for the synthesis of platinum-cobalt intermetallic nanoparticles for electrocatalytic applications

Journal:	*ChemComm*
Manuscript ID	CC-FEA-02-2023-000590.R1
Article Type:	Feature Article

Design principles for the synthesis of platinum-cobalt intermetallic nanoparticles for electrocatalytic applications

Siying Yu and Hong Yang*

Department of Chemical and Biomolecular Engineering, University of Illinois at Urbana-Champaign, 206, Roger Adams Laboratory, 600 South Mathews, Urbana, IL, 61801, USA

*: Corresponding author email: hy66@illinois.edu

Submitted as an invited Feature Article to *Chem. Commun.*

ABSTRACT

As the development of polymer exchange membrane fuel cells (PEMFCs) speeds up in recent years, producing active and durable electrocatalysts become an increasingly important technical challenge. Platinum-cobalt (Pt-Co) alloy electrocatalyst has been commercially applied to hydrogen-powered fuel cell vehicles, and their intermetallic forms promise better durability, which is crucial to satisfy the 8000-hour lifetime target of heavy-duty vehicles and other transportation options. In this feature article, we first present the atomically ordered structures of Pt-Co intermetallic, then discuss the thermodynamic and kinetic driving forces for making the PtCo-based intermetallic nanoparticles with desired structural attributes, followed by recent examples to illustrate how to achieve a better control in composition, size, and shape. Discussion on relationship between the key structural features and catalytic performance is focused on the application of Pt-Co intermetallic nanostructures as oxygen reduction reaction (ORR) electrocatalysts for hydrogen-powered PEMFCs. We emphasize specifically the importance of intermetallic structures for enhancing the durability and summarize the characterizations of their electrocatalytic performance in both three-electrode system and full cell studies. Finally, we provide our perspectives on the design, synthesis, characterization, and property studies of Pt-Co intermetallic nanoparticles as ORR electrocatalysts. This article should provide new understandings on the designs of ORR electrocatalytic applications using this class of intermetallics.

1. Introduction

Precious metals like gold (Au), silver (Ag), and platinum (Pt) have long been recognized as valuable elements since ancient times. In modern days, their excellent stability, unique surface-related physiochemical properties, and biocompatibility ensure they continue to play critical roles in a range of important industrial applications, such as petroleum cracking,[1] exhaust treatment,[2] nanomedicine,[3] and lately electrocatalysis for sustainability.[4-8] Among the precious metals, Pt-based materials have exhibited superior activitiy[4, 9, 10] and better durability[11, 12] when catalyzing oxygen reduction reaction (ORR),

which is the cathodic half-reaction in polymer exchange membrane fuel cells (PEMFCs) for hydrogen-powered transportation applications.

As the need for large PEMFCs surges, targeting the heavy-duty applications,[13] it becomes an acute issue to utilize Pt most effectively. Incorporation of early transition metals (*i.e.*, Fe,[14, 15] Co,[16, 17] Ni,[18, 19]) and nano-engineering of Pt-based electrocatalysts are the key technological solutions.[16, 19-23] Platinum-based bimetallic nanoparticles (NPs) often exhibit higher ORR activity than pure Pt electrocatalysts, in part because of the strain and ligand effects.[24, 25] Alloying with a 3d transition metal shifts the *d*-band of Pt downwards,[26] decreases its adsorption energy of oxygen species on surfaces,[27] lowers the activation energy barrier and, as a consequence, enhances the ORR performance.

Nanostructures of Pt-based bimetallic NPs directly affect their electrocatalytic properties. Upon the completion of initial activation, these electrocatalysts often have an alloy (or intermetallic) core and Pt-rich shell, or skin layer, which is regularly observed under scanning transmission electron microscope (STEM).[28, 29] The formation of Pt shell is due to the leaching of non-noble metals under acidic operating conditions,[30] and through the diffusion of Pt atoms with or without thermal treatment.[31, 32] The Pt skin not only serves as a protective layer against further dissolution, but also induces surface strain from the lattice mismatch with underneath alloy (or intermetallic) cores.[30, 33, 34] Besides composition and surface structures, nanoengineering is often used to control the particle size, which impacts more than the improvement of atomic utilization of precious metals. There is a tradeoff between increasing specific surface area to expose more active sites and decreasing surface energy to improve the structural stability. The optimal size for Pt-based bimetallic NPs was found to be around 5 nm, which exhibits the peak catalytic activity,[35] and may possess an oxophilic surface layer (PtO_x) to inhibit further metal dissolution during the cell operations.[36]

While the recent research has drastically improved the ORR activity of Pt-based electrocatalysts through the control of composition, size, and shape, a major challenge for their applications especially in heavy-duty areas, rises from the chemical and structural instability of Pt-based alloy NPs under harsh PEMFC operational conditions. A variety of Pt-based alloy electrocatalysts exhibit an ORR mass activity of >0.44 A/mg_{Pt} the

benchmark value set by the Department of Energy (DOE)[37] using the rotating disk electrode (RDE) technique after the standard accelerated stress tests (ASTs, typically for 30k cycles).[38] However, only a small portion of these electrocatalysts can retain high performance (>0.44 A/mg_{Pt}) in membrane electrode assembly (MEA).[16, 39] Among them, Pt-Co alloy electrocatalyst has been used in the hydrogen-powered fuel cell vehicles.[40] Thus, Pt-Co-based intermetallic, which exhibits long-range atomic order, is considered as a promising electrocatalyst to meet the DOE performance target of 8000-h system durability for PEMFCs used in heavy duty vehicles.

In this feature article, we start with the analysis of structures of Pt-Co intermetallics, followed by discussions of thermodynamic and kinetic factors in controlling the production of intermetallic NPs. Recent examples on how to control composition, size and shape and their applications in electrocatalysis will then be presented. It should be noted that there are reviews on Pt-based alloy and intermetallic nanoparticles published previously[8, 20, 41-52] and this feature article is focused on Pt-Co intermetallic NPs. Papers on Pt-Co alloys are largely not included in this feature article.[7, 53] Strictly speaking, intermetallic is a compound, in which a high exothermicity occurs in the formation of two metals and possesses different physical and mechanical properties (*e.g.*, brittleness, hardness and high melting point) than its alloy counterpart in bulk, we however focus on the atomic structure of the nanoparticles. Thus, we adopt the convention of using X-ray diffraction (XRD) as the method to characterize if a Pt-Co bimetallic nanostructure exists as intermetallic or not.

2. Structures of platinum-cobalt intermetallic nanoparticles

The primary difference between alloy and intermetallic is atomic ordering. Alloy is a disordered solid solution consisting of two or more metal elements with flexible, non-stoichiometric ratios. Structures of alloys may be determined by the symmetry of constituent metals that randomly occupy the lattice points of a crystal. For example, Pt-Co alloys have face-centered cubic (*fcc*) structure, the same as that of *fcc* phase of Pt or Co metal. On the other hand, intermetallic is composed of ordered array of metals atoms sitting on the lattice points, forming a compound of the constituent metals with long-range ordering. The stoichiometry of intermetallic is well-defined. In this context, each

intermetallic phase can be regarded as a new compound with a well-defined unit cell that may be identified by a distinctive XRD pattern.

Figure 1a illustrates the unit cell structures and low-index facets of three Pt-Co intermetallic structures: $L1_2$-Pt_3Co, $L1_0$-PtCo, and $L1_2$-$PtCo_3$. $L1_0$-PtCo has the tetragonal crystalline phase, in which layers of Pt and Co atoms stack alternatively along *c* axis. The $L1_2$ structure exists in a cubic phase, with one type of metal atoms occupying all six face centers and the other one occupying all eight corners. These intermetallic compounds exhibit very different XRD patterns when compared with Pt, thus XRD is the most efficient and straightforward method to characterize the Pt-Co intermetallics (**Figure 1b**). In this article, XRD characterization is used as the indicator of the formation of intermetallic and the determination of their specific structures ($L1_0$ or $L1_2$).

Figure 1c illustrates the typical Pt-Co phase diagram drawn based on theoretical calculation.[54] The most commonly observed Pt-Co intermetallic phases are $L1_0$-PtCo and $L1_2$-Pt_3Co, respectively. While $L1_2$-$PtCo_3$ has been predicted by simulation,[54] there is sparse experimental observation.[55-57] In this perspective, we will cover primarily the $L1_0$-PtCo intermetallic, and to a lesser degree, the $L1_2$-Pt_3Co phase, because of their applications in electrocatalysis.

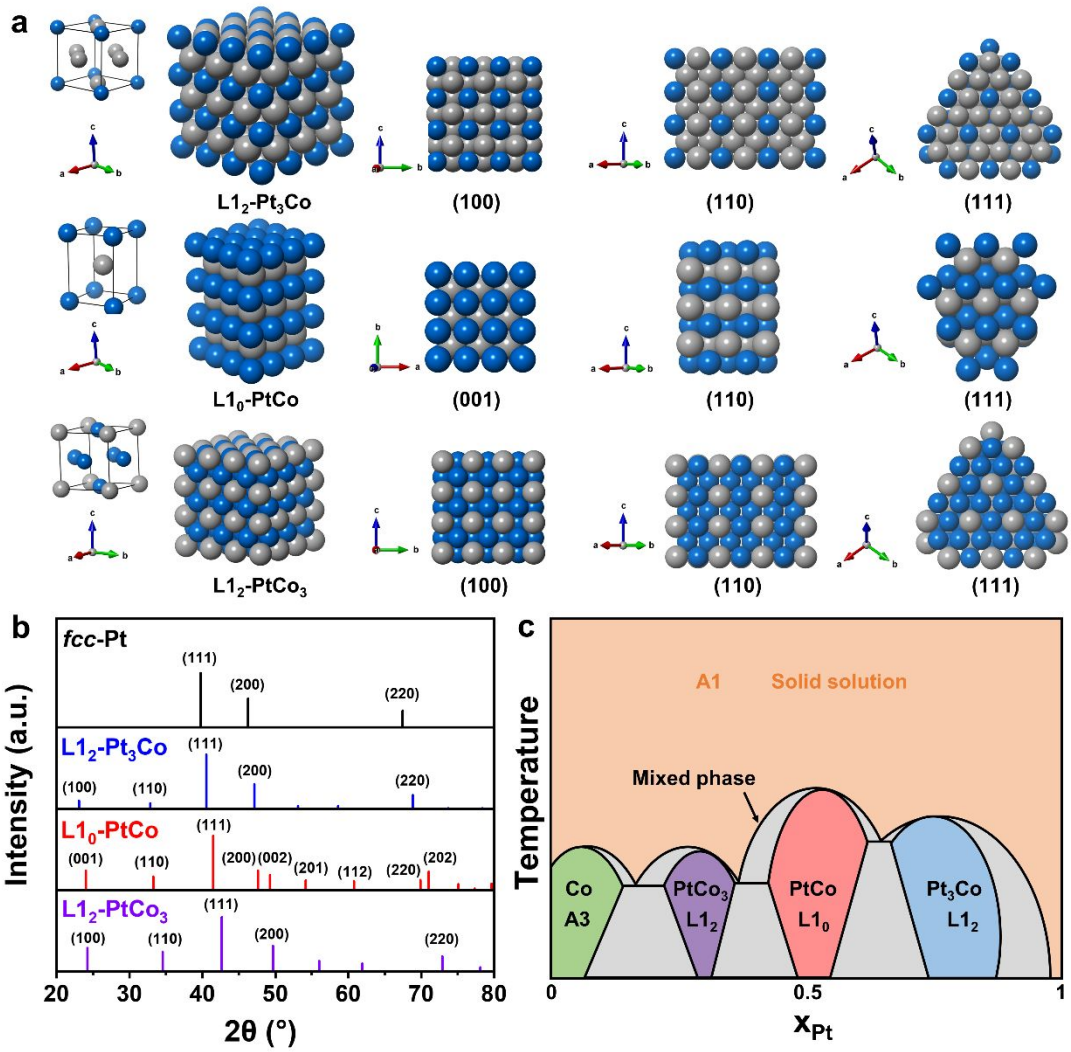

Figure 1. Illustrations of $L1_2$-Pt_3Co, $L1_0$-PtCo, and $L1_2$-$PtCo_3$ intermetallics: (a) Unit cell, atomic packing, and low-index facets (color code: blue-Co, grey-Pt), (b) XRD patterns for *fcc*-Pt (PDF#04-0802), $L1_2$-Pt_3Co (PDF#29-0499), $L1_0$-PtCo (PDF#43-1358), and $L1_2$-$PtCo_3$ (obtained from VESTA simulation, using unit cell parameters from reported $PtCo_3$ alloy structure[58]), and (c) conceptualized Pt-Co phase diagram.

3. Design principles for the synthesis of Pt-Co intermetallic nanoparticles

3.1. Thermodynamic and kinetic driving forces

Platinum-cobalt intermetallic nanoparticle is typically made from its alloy counterpart through thermal treatment.[30, 59] The thermodynamics for making intermetallic from alloy

via such treatment can be understood based on the change of Gibbs free energy of the ordering process (ΔG_o) at given temperature (T), which can be written as:

$$\Delta G_o = \Delta H_{a\to i} - T\Delta S_{a\to i} \quad (1)$$

where $\Delta H_{a\to i}$ is the change of enthalpy and $\Delta S_{a\to i}$ is the change of entropy from disordered alloy (a) to ordered intermetallic (i) phases. For alloy and intermetallic with the same constituent metals and stoichiometry, $\Delta H_{a\to i}$ is negative for this process due to the stronger Pt-M bonds in an ordered array (intermetallic) than that in a random array (alloy).[43, 44] $\Delta S_{a\to i}$ is negative as well, because entropy is interpreted as the degree of disorder or randomness in the system. Thus, the less disordered structure has a smaller value of S. Since temperature (T) is in unit of K, the second term ($-T\Delta S_{a\to i}$) is positive and its value increases monotonically with elevated temperature. The relationship between ΔG_o and T can be conceptually depicted (**Figure 2**). The ordering process is thermodynamically favored when the value of T satisfies the condition: $\Delta G_o < 0$. In another word, when temperature is high enough, thermodynamically stable structure is alloy, which explains the "A1 solid solution" area in the Pt-Co phase diagram (**Figure 1c**).

The value of T at the critical point where ΔG_o is zero is defined as the critical phase-transition temperature (T^c), below which the intermetallic structure is energetically favored (**Figure 2**, the coordinate on the left). When size is reduced to nanometer scale, surface energy must be taken into consideration because of the dramatic increase in number of surface dangling bonds and specific surface area. Thus, the extra surface energy term ($A\Delta\gamma_{a\to i}$) needs to be added to calculate the ΔG_o value for this process:

$$\Delta G_o = \Delta H_{a\to i} - T\Delta S_{a\to i} + A\Delta\gamma_{a\to i} \quad (2)$$

where A is the surface area and $\Delta\gamma_{a\to i}$ is the change of surface energy. Intermetallic has higher surface energy than alloy due to the higher bond energy, resulting in a higher value of ΔG_o for a given temperature, which narrows the feasible temperature range of ordering process. As is shown in **Figure 2**, the critical phase-transition temperature of nanomaterial

(T^c_{nano}) is smaller than that of bulk material (T^c_{buk}). More importantly, for a given T, the increased $\Delta G_o(T)$ implies a smaller energy drop (equal to the absolute value of ΔG_o), which makes the intermetallic structure less thermodynamically favorable at the same temperature (**Figure 2**, the coordinate on the right). Thus, synthesis of Pt-based intermetallic NPs often requires additional annealing step to overcome the activation energy barrier (E) from disordered to ordered structure.

Dependence of reaction rate on temperature can be described by the logarithmic analysis. A simplified kinetic model of disorder-to-order transition can be treated as a combination of new phase formation within the parent phase (nucleation) and material transport (diffusion).[44] Thus, the overall rate for the formation of intermetallic from alloy can be written as the product of new phase formation rate $f(T)$ and diffusion rate $D(T)$:

$$R(T) = f(T)D(T) \quad (3)$$

The new phase formation rate $f(T)$ is closely related to the formation energy of intermetallic, while the diffusion rate $D(T)$ depends on atom-exchange mechanisms. Under the assumption that diffusion of metal atoms can be regarded as a simple lattice jump from their original positions to neighboring vacancies, an intermetallic structure with relatively weak Pt-M bond tends to have both low defect formation energy and low jumping barrier.[44] The atom diffusion may significantly accelerate when reaction temperature rises. This model may be sufficient to understand the general formation, understanding the local ordering mechanism at atomic scale however still requires advanced experimental techniques, such as high resolution *in-situ* microscopy, which enable the characterization of the Pt-Co ordering process (see examples discussed in section 3.2).

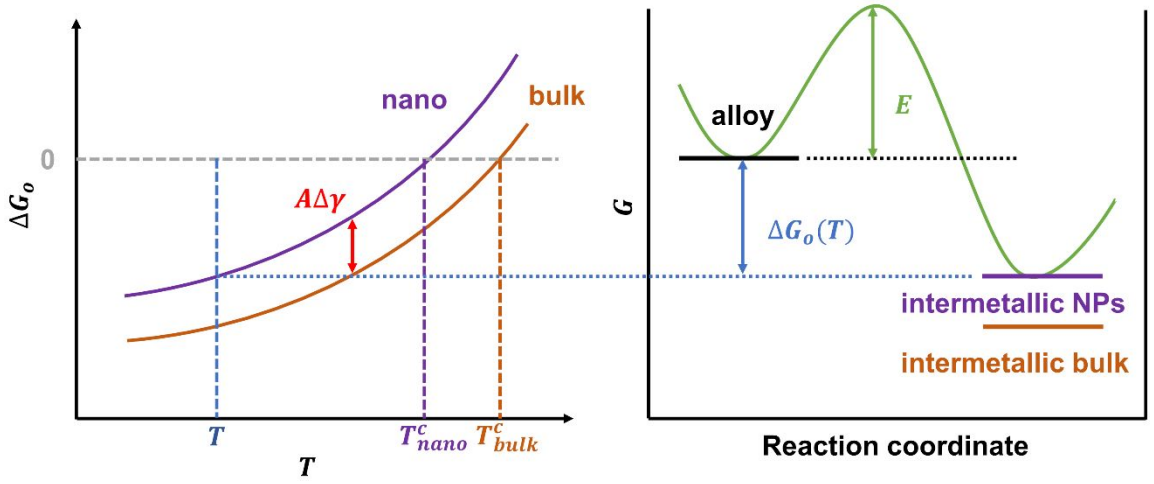

Figure 2. Illustration of change in Gibbs free energy of the process of atomic ordering (ΔG_o) from alloy to intermetallic phases and the corresponding reaction coordinates.

3.2. Atomic ordering

At the atomic scale, formation of intermetallic phase corresponds to the ordering of atoms at a long coherent length. An intermetallic structure is thermodynamically stable below the critical temperature (T^c) but requires activation energy to complete the disorder-to-order transition. It is rare to obtain a perfectly ordered intermetallic structure since most Pt-Co intermetallic NPs inevitably contain disordered regions. Thus, degree of ordering (S^2) is used to quantitatively describe the transition from alloy to intermetallic phase. Experimentally, the degree of ordering (S^2) may be estimated based on XRD data using the following equation:[60, 61]

$$S^2 = \frac{\{I_{110}/I_{111}\}_{measured}}{\{I_{110}/I_{111}\}_f} \quad (4)$$

where $\{I_{110}/I_{111}\}_{measured}$ and $\{I_{110}/I_{111}\}_f$ are the integrated intensity ratios between (110) and (111) diffractions obtained from the measurement of a sample and the simulation of fully-ordered intermetallic ($L1_0$ or $L1_2$ for Pt-Co) phase, respectively. The degree of ordering is an important structural factor when evaluating the structural properties, as it affects the activity,[60, 62] and durability[61] of Pt-Co intermetallic NPs as electrocatalysts.

The ordering process is often studied by using high-resolution microscopic characterization techniques. High-resolution transmission electron microscopy (TEM) study can be used to examine dynamics of a range of Pt bimetallic nanostructures and provide critical clues and details for developing the proper processes.[31, 32, 61, 63-69] Recent *in situ* TEM study reveals the continuous but distinctive stages of surface rearrangements to form intermetallic phase during the annealing of Pt_3Co nanoparticle: (1) initial alloy elemental distribution, (2) formation of surface Pt-skin layer, (3) nucleation of structurally ordered domains, and (4) development of ordered framework.[32] Segregation of Pt onto the surface was highly sensitive to the annealing temperature. It was driven by a negative enthalpy for surface segregation when below 550 ° C. With annealing temperature increased, the disorder-to-order transformation initiated on the Pt_3Co {110} facets, which had the largest driving force according to density functional theory calculations. The newly formed ordered structure then continued to propagate on {001} planes inwards to the center of the nanoparticle.

Besides the mode of formation through continuous evolution, phase transition to intermetallic may compete with surface diffusion in the ordering process, as being observed in the synthesis of $L1_2$-Pt_3Co NPs.[63] The two formation modes are surface diffusion-induced phase transition (SDIPT) and reconstruction-induced body phase transition (RIBPT). SDIPT occurred mainly on the surface layer, involving a long-range diffusion driven by the surface chemical potential gradient, while RIBPT referred to atomic reconstruction inside the crystal within a short range. These two competing modes could work synergistically to produce $L1_2$-Pt_3Co structure with different morphologies. When Pt_3Co alloy nanoparticles went through low-temperature diffusion annealing process (LTDAP) and reached 600 ° C, the process occurring on {100} facet could be categorized into three stages according to the growth rate of intermetallic in the two formation modes: (1) SDIPT-dominated stage, (2) SDIPT and RIBPT competitive stage, and (3) RIBPT-dominated stage. Depletion of low-coordination (CN) surface atoms decelerated SDIPT in the later stages, and RIBPT gradually took over after the energy for short-range reconstruction became larger than the barrier of nucleation in the second stage (**Figure 3a**). For {110} facet, however, corner atoms preferred to move away from the site instead of

undergoing phase reconstruction in the first stage. This process was called “low-coordination (CN) atom losing stage”. The loss of atoms at the corners left behind large amounts of defects and vacancies, leading to the defect-driven rapid growth at the second stage. As a consequence, the phase reconstruction also became easier than before, because of rich defects and vacancies in the second stage. The third stage is RIBPT-dominated slow growth, as the intermetallic region propagated inwards with diminishing vacancies and defects. If Pt_3Co alloy nanoparticles were treated via the direct high-temperature annealing process (DHTAP) at 700 ° C, the ordered phase started to form at the outermost later of {100} facet (**Figure 3b**), but intermetallic growth on {110} facets slowed down. In general, SDIPT under DHTAP conditions was slower than RIBPT, and the corners atoms did not have sufficient time to diffuse onto {100} facets. This sluggish diffusion under DHTAP resulted in more corner atoms than LTDAP, thus cubic and spherical products were generated, respectively (**Figure 3c**).

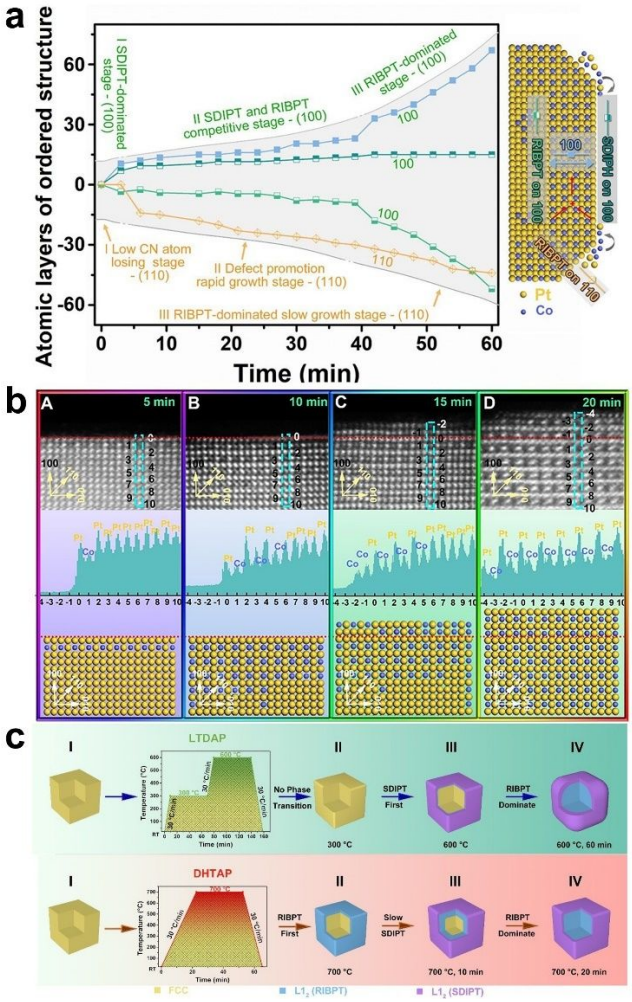

Figure 3. Reconstruction and surface-diffusion-induced phase transition behavior along the [100] and [110] directions of Pt_3Co intermetallic. (a) Changes of atomic layers of the ordered $L1_2$-Pt_3Co intermetallic nanocrystals as a function of time along the two directions. (b) Layer-by-layer growth of the ordering Pt_3Co during annealing. Enlarged high-angle annular dark field (HAADF)-STEM images of the {100} surface, the intensity profiles taken from the surface marked by rectangles and the corresponding atomic model of enlarged HAADF-STEM images acquired at 700 ° C for (A) 5 min, (B) 10 min, (C) 15 min, and (D) 20 min. (c) Schematic representation of the dynamic process of Pt_3Co cubes under LTDAP and DHTAP, respectively. Reproduced with permission from ref. 63. Copyright 2021, American Chemical Society.

Besides atomic ordering from Pt-Co alloy NPs, the formation of intermetallic structure can also be the result of the diffusion of Co atoms into Pt NPs.[64] CoN_4-rich carbon (Co/NC)

was shown to be a viable precursor and could be prepared from zeolitic imidazolate framework-8 (ZIF-8). This precursor was used as both the support and the Co source (**Figure 4a**). At the mass loading of 20 wt.%, Pt NPs formed on the CoN_4-rich carbon and subsequently alloyed with Co atoms. STEM-energy-dispersive X-ray (EDX) mapping study indicates that as temperature increased from room temperature to 1000 ° C, Co atoms gradually diffused into the lattice of Pt NPs (**Figure 4b**). The atomic ratio between Co and Pt increased eventually to ~0.3 (**Figure 4c**). This observation confirmed Pt-Co intermetallic NPs could be made through diffusion of Co atoms into Pt NPs as well. *In-situ* environmental TEM was used to examine the atomic ordering, including the study of mechanisms of metal segregation and particle coalescence.[31, 32, 65, 70]

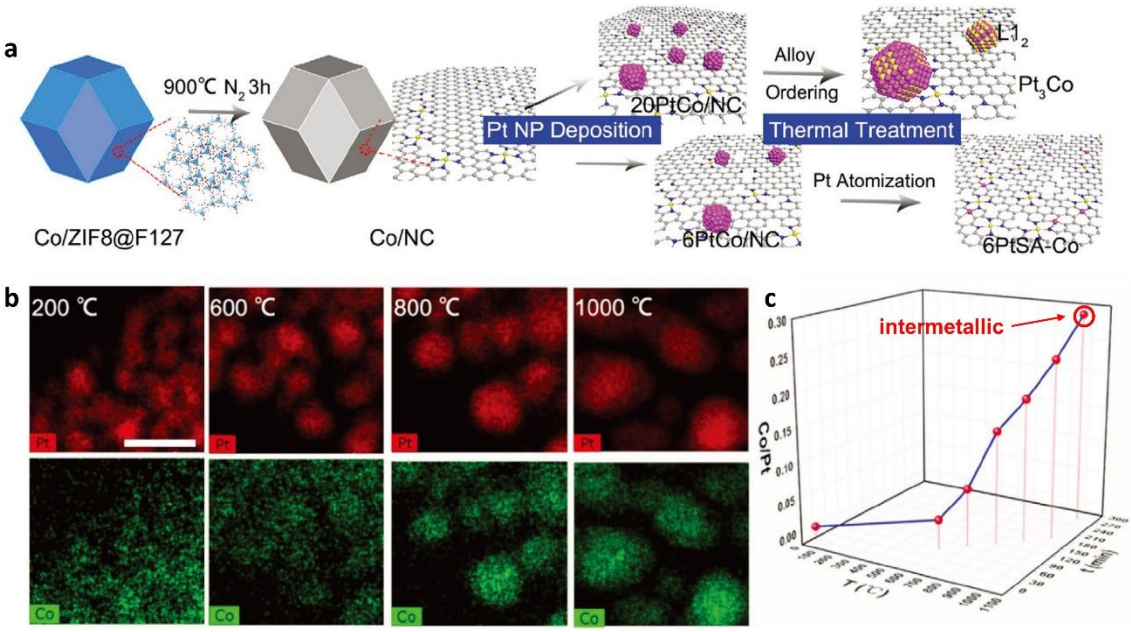

Figure 4. (a) Schematic illustration showing the synthesis of PtCo/NC (*n*PtCo/NC, *n* represents the mass loading of Pt, *n*=20 or 6 wt.%). Observation of the dynamic process of alloying between Pt and Co during the thermal treatment: (b) EDX mapping of Pt (red) and Co (green) species in the 20PtCo/NC sample after annealing at 200, 600, 800, and 1000° C, respectively (scale bar: 10 nm). (c) Atomic ratio between Co and Pt as functions of temperature and time. Reproduced with permission from ref. 64. Copyright 2021, Wiley-VCH.

3.3. Composition control

In principle, it is easier in controlling the composition of intermetallics than alloys in the formation of Pt-based bimetallic NPs,[71] because stoichiometry of intermetallic is well defined.[72] In practice, a stoichiometric ratio obtained from the phase diagram might still be locally inhomogeneous.[44] Metal segregation,[73] especially surface segregation of Pt, is a commonly observed phenomenon. Surface segregation often occurs after heat[28, 29, 31, 65] or acid treatment[30] of Pt-based bimetallic. The formation of Pt-rich shell changes the overall stoichiometric ratio for the intermetallic NPs. The existence of Pt shell however can be beneficial, because this surface structure may improve both the activity and durability of electrocatalysts.[30, 33, 34] Controlling the feeding ratio thus is needed to achieve the required stoichiometry with Pt-enriched skin layer or shell.[44, 74]

For Pt-Co, the two most commonly observed intermetallic phases are $L1_0$-PtCo and $L1_2$-Pt_3Co. Theoretical simulation suggests these two intermetallic structures are energetically favored in the similar temperature range (**Figure 1c**).[54] As a result, the procedures for making either intermetallic can be similar, except for the amount of metal precursors added to the synthetic mixture.[33, 75] $L1_2$-$PtCo_3$ has been theoretically proposed but with few experimental observations.[56, 57] Small $L1_2$-$PtCo_3$ intermetallic NPs on carbon were obtained by spray dehydration, followed by annealing.[55] XRD pattern was used to determine the formation of this intermetallic phase by comparing it with the standard diffraction pattern from $L1_2$-$PtFe_3$ (PDF#71-8365). A slight positive shift in 2θ angle was observed, because Co has a smaller atomic radius than Fe. The $L1_2$-$PtCo_3$ intermetallic NPs are hard to produce, presumably because Co prefers to exist in *hcp* phase at ambient temperature, which has a large lattice mismatch with *fcc* Pt. It should be noted that the stoichiometric ratio of the final product is helpful to verify the intermetallic structure, but it does not necessarily imply whether the intermetallic is $L1_0$-PtCo, $L1_2$-Pt_3C, or $L1_2$-$PtCo_3$. Both metal segregation and local inhomogeneity can lead to an intermetallic structure with very different Pt/Co ratio.[76] It is a common practice to use XRD to characterize and confirm the crystal structures of the Pt-Co intermetallics, and rely on high resolution STEM for detailed atomic information. It is noteworthy an intermetallic does not follow the

relationship between lattice parameters and atomic content as defined by the Vegard's law for a solid solution (*i.e.*, random alloy). Even if the composition is nonstoichiometric, Pt-Co NPs can still show intermetallic features in characterization, such as XRD.

A third metal can be added to a Pt-Co intermetallic to modify its surface and core structures, thus catalytic properties. The incorporation of additional metal(s) into the crystal lattice raises a question whether such NPs can still be called "intermetallic", since strictly speaking, at least one lattice site no longer has the long-range ordering or specific stoichiometry in the bimetallic structures as shown in **Figure 1a**. In this feature article, we coin the term "half-intermetallic" to describe a ternary or multi-metallic system, in which one lattice site (*i.e.*, Pt) is fully ordered, while the other lattices site is occupied by the secondary metal atoms (*i.e.*, non-Pt metals) that can be randomly distributed.[77-79] The amount of the incorporated metal is typically small (<10 at%). For example, tungsten (W) atom was reported to be incorporated into $L1_0$-PtCo NPs to form a half-intermetallic of $W_{0.05}PtCo$.[80] Theoretical calculations and extended X-ray absorption fine structure (EXAFS) analysis revealed that W atoms stabilized the intermetallic structure and tuned the Pt-Pt distance and changed its binding energy with oxygen species. The incorporation of Cu into $L1_0$-PtCo intermetallic was also reported to form a half-intermetallic $PtCo_xCu_{1-x}$ (x=0.25, 0.5, 0.75).[81] A rationale for making half-intermetallic is to tune the Pt-Pt distance to improve its catalytic activity.

3.4. Size control

Size plays important roles in determining the properties of Pt-based intermetallic NPs.[82] Small NPs have high specific surface area that often results in exposing large population of active sites. However, when size is too small (diameter <~2 nm, assuming a spherical shape), the performance may suffer as well. Finding the optimal size is to balance the catalytic activity and durability. [35, 36] For Pt-Co intermetallic NPs, there also exists a size-dependent structural ordering.[83-85]

While controlling size of bimetallic alloy may be straightforward, it can be challenging for intermetallic NPs since high-temperature annealing (>500 ° C) is generally required to

overcome the energy barrier for atomic ordering.[86] Based on Gibbs-Thomson equation, the chemical potential of surface region of a nanoparticle (μ) can be written as:

$$\mu = k_B T ln[c_{eq}(r)] = \frac{2\sigma v_{at}}{r} \ln [c_{eq}(\infty)] \quad (5)$$

$$c_{eq}(r) = c_{eq}(\infty) \exp \left(\frac{2\sigma v_{at}}{r k_B T}\right) \quad (6)$$

where $c_{eq}(\infty)$ is the solubility of atoms taken from an infinite flat surface, σ is the surface tension, v_{at} is the atomic volume, r is the surface curvature and k_B is the Boltzmann constant. The reciprocal relationship between chemical potential μ and surface curvature r implies atoms tend to diffuse to surfaces with large curvature radius. Ostwald ripening and particle coalescence[87] may happen simultaneously during the process, resulting in the formation of polydisperse and larger intermetallic NPs. The key to size control, based on the discussion above, is to inhibit the atomic diffusion and particle migration during the heat treatment process. For Pt-Co intermetallic NPs, enhancing support-metal interaction and applying spatial confinement are two main approaches to the size control. Both methods promote the uniform dispersion of metal precursors.

3.4.1. Support-metal interaction

Electrostatic adsorption of ions on protonated or charged surfaces can enhance support-metal interaction.[59, 88] Fine $L1_0$-PtCo intermetallic NPs were made through anchoring metal complexes on N-doped carbon using the strong electrostatic adsorption (SEA) technique.[59] This anchoring effect provides locally stabilized metal species, preventing atoms from migration and aggregation during mixing and heating process. The surface of the support could be either positively or negatively charged by adjusting pH values in either side of the point of zero charge (PZC) (**Figure 5a**). The metal precursors with the opposite-charges electrostatically adsorbed onto the surface. One advantage of electrostatic adsorption is that the support-metal interaction is tunable by adjusting pH value. **Figure 5b** shows pH-dependence of size-tunable PtCo alloys NPs. When pH value becomes smaller, the surface of the support is more protonated. As a result, Pt and Co precursors have strong affinity to

the support, resulting in the formation of small NPs. After atomic ordering through heat treatment, $L1_0$-PtCo NPs formed, as being characterized by XRD (**Figure 5c**). The alternating layers of Pt and Co atoms could be observed in TEM micrograph (**Figure 5d**). The average size of these PtCo intermetallic NPs could be as small as sub-3 nm, meanwhile maintaining a narrow size distribution (**Figure 5e**).

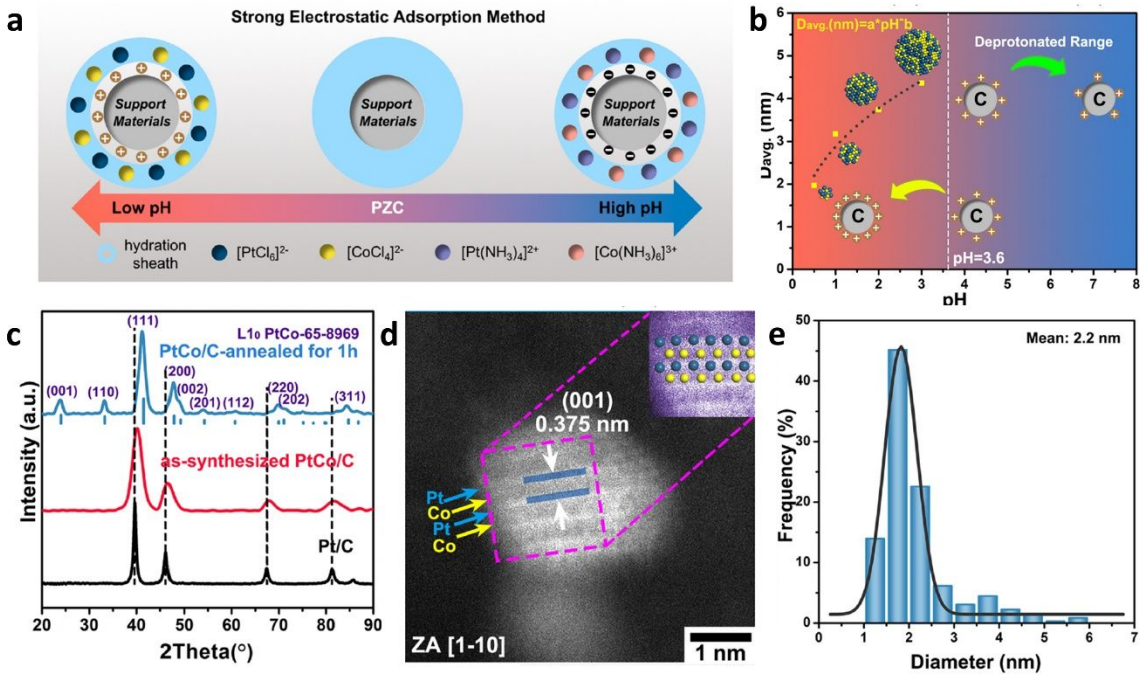

Figure 5. (a) Schematic illustration of the SEA method for preparing bimetallic PtCo NPs on the N-doped carbon support in different pH ranges. A hydration sheath with the electrostatically adsorbed Pt and Co complexes formed on the surface by adjusting the pH value of the environment. (b) Illustration of effect of surface charges and the fitted curve of average diameter as a function of pH value of the A1-PtCo NPs. (c) XRD pattern, (d) HAADF-STEM image with a false-color enlargement (inset), and (e) size distribution analysis of the $L1_0$ phase intermetallic NPs. Reproduced with permission from ref. 59. Copyright 2021, Elsevier.

Electron-rich elements (S, N, O) that coordinate with Pt atoms are often incorporated into carbon support to enhance the support-metal interaction.[89-91] Porous S-doped carbon (S-C) support was prepared by cobalt-assisted carbonization of molecular precursors with silica

NPs as templates.[89, 90] Metal salt precursors were impregnated onto the S-C supports with total metal contents 20 wt.% and underwent high-temperature H_2-reduction treatment to produce intermetallic NPs (**Figure 6a~c**). Both $L1_0$-PtCo and $L1_2$-Pt_3Co intermetallic NPs could be produced using this method (**Figure 6d and e**). Broad peaks in XRD patterns suggest these NPs have small crystal domains. Size analysis based on microscopic characterization further confirmed the average size was typically less than 5 nm for these NPs (**Figure 6g and f**). Instead of using premade S-doped carbon support, S-C support could form *in-situ* during the atomic ordering step under the heat treatment. A molecule-assisted approach was reported in producing carbon supports doped with heteroatoms (S, N, O).[91] Molecular additives such as sodium thioglycolate (STG) were introduced into the mixture of carbon support and metal precursors. Heteroatom-doped graphene layers formed during the heat treatment and suppressed alloy sintering and particle growth of intermetallic. In general, enhanced support-metal interaction is effective in size control, though it could be detrimental for atomic ordering. For instance, the strong metal-S interaction suppressed not only the inter-particle sintering but also intra-particle ordering, which restrained the formation of ordered structure.[89]

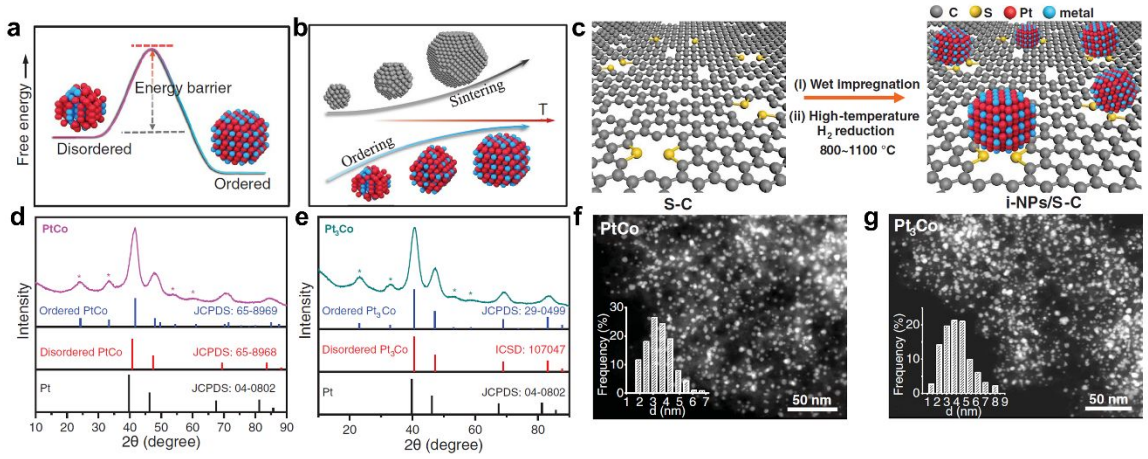

Figure 6. Schematic illustrations showing (a) the kinetic energy barrier for atom ordering in the disorder-to-order transition, and (b) the dilemma of simultaneously accelerated sintering kinetics and atom ordering kinetics with temperature. (c) Schematic illustration of the high-temperature sulfur-anchoring approach. XRD patterns of (d) PtCo, and (e) Pt_3Co intermetallic NPs. The standard peaks for Pt and ordered and disordered PtCo/Pt_3Co are also shown. Asterisks mark the characteristic superlattice peaks of ordered intermetallic

structures. HAADF-STEM images of (f) PtCo, and (g) Pt_3Co intermetallic NPs (inset: particle size distribution). Reproduced with permission from ref. 90. Copyright 2021, American Association for the Advancement of Science.

3.4.2. Spatial confinement

Preventing atomic diffusion onto surface may inhibit unwanted particle growth through confinement. Protective layer may be used, but it raises a concern that the layer itself may block active sites on intermetallic NPs. Removal of protective layers is often necessary to activate catalysts if such strategy is used.[92, 93] For example, 3 nm $L1_0$-PtCo intermetallic NPs can be synthesized via a surface coating strategy.[76, 93] The dopamine coating was firstly introduced on the carbon supported Pt NPs via π-π bond conjugation, and subsequently converted into carbon shell, resulting in the adsorption of Co ions.[93] Silica coating was then applied to the surface to prevent particle sintering during annealing. Such rigid silica shell is effective in limiting the size growth, but it also requires HF etching in the post-treatment steps. As a comparison, carbon shell can be easily removed by air etching.[15, 92]

Other than protective layers, certain support is capable of spatial confinement by itself. For example, porosity of mesoporous carbon helps to control particle size.[33, 78, 94] The synthesis procedures are generally similar to those non-porous systems. Mesoporous carbon support is firstly obtained by annealing of ZIF-8 or its derivatives. The metal precursors are impregnated onto the mesoporous carbon and the mixture is dried either by heat treatment or freeze drying.[78, 94, 95]

3.5. Morphological control

The necessity for controlling the shape stems from the requirement for understanding structure-property relationship in order to design the electrocatalysts with high performance. For catalytic property, surface and near surface structures[96] of Pt-based bimetallic intermetallic NPs are particularly important. Surface structure and shape of Pt-Co intermetallic NPs are highly correlated since the shape of nanostructure is determined thermodynamically by surface energy, and kinetically by relative growth rates of different facets. In addition, the surface energy is affected by local environment and differs among

different facets under different reaction systems. Low-index facets of crystals are often exposed due to their low surface energy and slow growth rate along their normal direction.

3.5.1. Shape and facet controls

Since most Pt-Co intermetallic NPs are produced by heat treatment, temperature is an important parameter to control the formation of exposed facets. The evolution of crystal facets could be studied by high resolution STEM.[32] In the disorder-to-order transition of Pt_3Co alloy NPs, the {110} planes were observed to be the main surface at 550 ° C. When temperature was raised to 600 ° C, however, {111} facets became dominant and ultimately grew to 2~3 unit cell thick at 700 ° C. As the temperature rose to 800 ° C, {110} facets formed again and the Pt_3Co intermetallic NPs evolved into truncated cuboctahedra shape. Since surface faceting is closely related to electrocatalytic properties, this work revealed that preferred facets can be exposed with judicious selection of processing temperature and other conditions.

Synthesis of octahedral $L1_0$-PtCo NPs with {111} facets predominantly was achieved by colloidal synthesis and subsequent annealing.[97] Pt-Co octahedral nanocrystals were firstly prepared in solution, followed by loading onto carbon supports. Atomic ordering was carried out in 4% H_2 at 600 ° C to convert alloy into $L1_0$-PtCo intermetallic. The formation of Pt skin was possible by depositing excess Pt at 80 ° C. The TEM micrograph shows the octahedral nanocrystals have uniform size and exhibit well-defined {111} facets, uniformly dispersed on carbon support (**Figure 7a-c**). The atomic resolution STEM image indicates that the nanoparticle was composed of a highly ordered $L1_0$-PtCo core with a smooth Pt shell of 3~4 atomic layers in thickness (**Figure 7d and e**). In order to obtain the {111}-enclosed octahedral nanocrystal, the growth pattern of Pt was controlled by adjusting the reaction rate ratio between atom deposition and surface diffusion (V_{dep}/V_{diff}). The deposition of Pt atoms was initiated on the {001} facets due to their higher surface energy than that of {111} facets. The Pt adatoms may migrate to the edges and {111} facets through surface diffusion. When $V_{dep}/V_{diff} \ll 1$, the growth was dominated by surface diffusion, allowing a uniform coating of Pt and ultimately, the formation of octahedral $L1_0$-

PtCo nanocrystal. Injection rate of precursors and rection temperature can both affect the reaction rate ratio (V_{dep}/V_{diff}).

Synthesis of Pt-Co intermetallic with high-index facets is non-trivial. Controlled synthesis of tetrahexahedral NPs is one of the few successful cases.[56] Density functional theory calculations show that surface modification by bismuth (Bi) stabilizes the {210} high-index facets and may result in tetrahexahedral NPs, regardless of their internal crystal structure. Without the modification by Bi, the specific surface energy is 1.70 J/m^2 for {111} facet and 1.42 J/m^2 for {001} facet. These values are smaller than those of high-index facets (*i.e.*, 2.27 J/m^2 for {210} facet and 2.44 J/m^2 for {201} facet), resulting in a truncated octahedron enclosed by {111}, {100}, {001} and {101} facets, as is suggested by Wulff theorem. Upon surface modification by Bi, the specific surface energy is expected to drop by ~90% for {210}, {102}, and {201} facets. Experimentally, pseudo-spherical PtCo alloy NPs successfully transformed into $L1_0$ phase intermetallic in tetrahexahedral shape with {210} surfaces, when they were annealed in Bi atmosphere.

While it is uncommon, one-dimensional nanowire consisting of $L1_0$-PtCo core[98] and Pt-rich surface was reported.[22] This nanostructure exhibits compressively strained high-index facets. The preparation was carried out using platinum acetylacetonate ($Pt(acac)_2$), $Co(acac)_2$ as metal precursors, along with cetyltrimethylammonium chloride (CTAC), glucose, oleylamine (OAm), and 1-octadecene (ODE). This mixture was treated in 5%H_2 at 550 ° C for atomic ordering. The $L1_0$-PtCo nanowire maintained its one-dimensional morphology after this process (**Figure 7f**). The green square in **Figure 7g** was the enlarged region in **Figure 7h** with corresponding fast Fourier transform (FFT), suggesting high crystallinity. Homogeneity of elemental distribution was demonstrated by EDX elemental maps (**Figure 7i**). Analysis of the inter-planar distance and the stepped atomic terminations suggested that the edges of the annealed nanowire possessed the high-index facets {221} and {211} (**Figure 7j**). The formation of nanowires required presence of both glucose and CTAC. Surface became smooth if CTAC was replaced with cetyltrimethylammonium bromide (CTAB). This observation indicates that the choice of halide played a role in the formation of high-index facets. Such one-dimensional structure provides high contact area with the carbon support and requires no protective layer to prevent agglomeration during

annealing. In this context, the nanowires seem to be thermally stable. The annealed nanowire formed thin Pt-rich layer, which enhanced its chemical durability as electrocatalysts. Besides the $L1_0$ phase, $L1_2$-Pt_3Co nanowires were prepared via nanometer (nm)-sized spatial confinement using mesoporous silica templates.[99] The porous templates allow the control over the size and shape of nanostructures and prevent agglomeration during the atomic ordering process at high temperature. The as-prepared Pt_3Co intermetallic nanowires were catalytically active in both alkaline hydrogen evolution reaction and acidic methanol oxidation reaction.

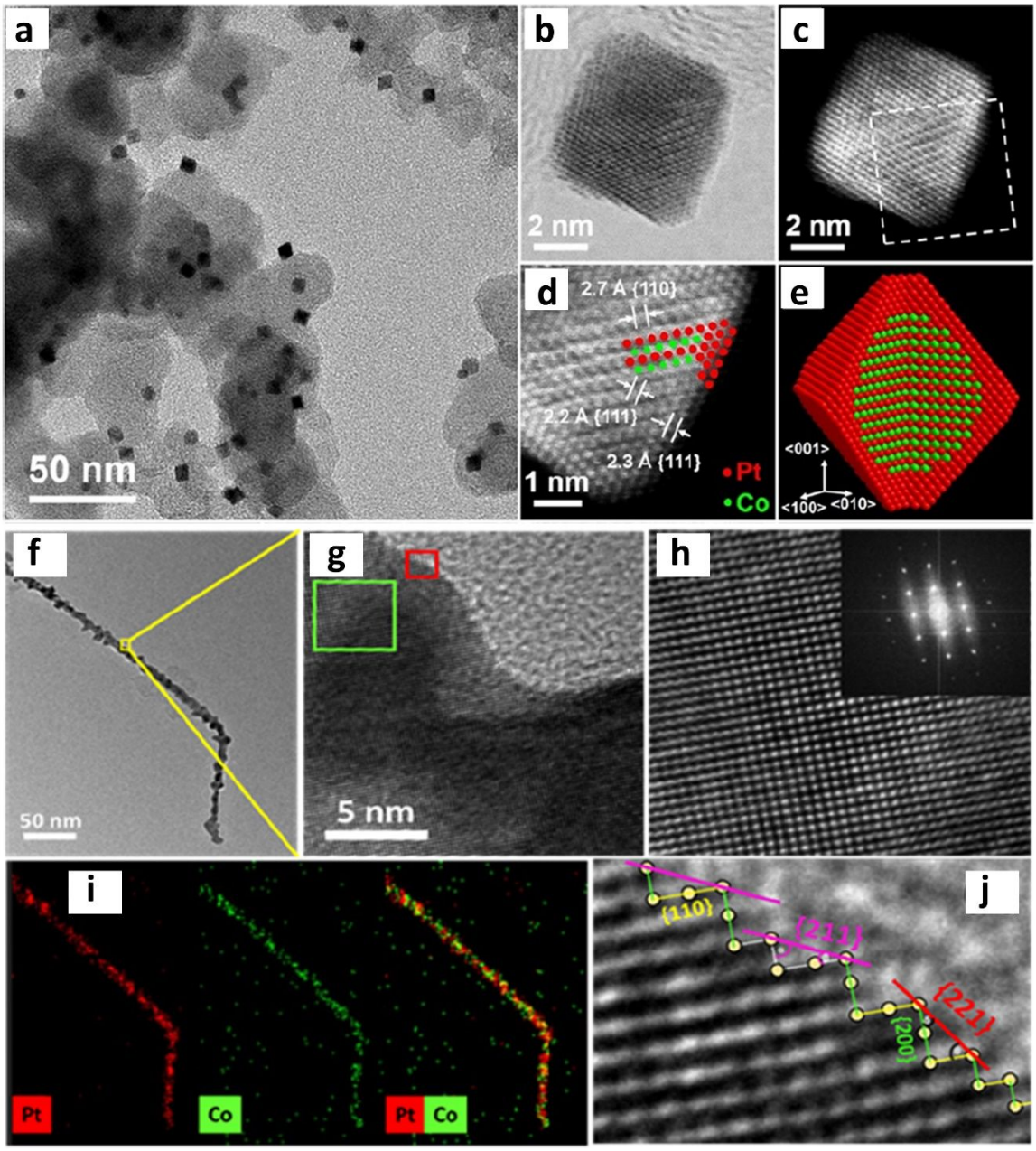

Figure 7. Characterizations of the *fct* Pt-Co@Pt octahedral nanocrystals supported on carbon. (a) TEM image, (b) high-angle annular bright field-, and (c) HAADF-STEM images of a nanocrystal along the [1-10] direction. (d) Atomic-resolution STEM image taken from the corner region marked by a box in panel (c). (e) Schematic of the nanocrystal featuring an intermetallic core, a Pt shell of about three atomic layers thick, and {111} facets. Reproduced with permission from ref. 97. Copyright 2021, American Chemical Society. (f) TEM image of PtCo/C NW annealed at 550 ° C, (g) the corresponding HR-

TEM image, (h) HR-TEM image and the FFT (inset) of the green box region in (g). (i) EDS elemental mapping, and (j) HR-TEM image of red box region in (g). Reproduced with permission from ref. 22. Copyright 2022, American Chemical Society.

3.5.2. Core-shell structure

Pt-Co intermetallic NPs often exist or are made in core-shell structures, typically with Pt shell.[100-104] Molecular dynamics simulations were carried out to compare the thermo-stability of Pt- and Co-coated $L1_2$-Pt_3Co NPs.[105] The simulated results suggest that Pt is much better than Co as the coating element for improving both structural and thermal stability of Pt_3Co NPs. Platinum shell was often observable directly using high resolution STEM.[28] Typically, such Pt shell contains 2 to 3 atomic layers and was strained by the ordered $L1_2$-Pt_3Co intermetallic core. Such core-shell structures could exhibit better durability than alloys, after potential cycling between +0.05 and +1.00 V for 5k cycles in 0.1 M $HClO_4$ solution. During the cycling, surface roughing and removal of contaminants could result in high electrochemical surface area (ECSA) in a short term, but only those NPs consisting of well-ordered Pt shell and $L1_2$-Pt_3Co intermetallic core possessed long-term stability in ECSA.

The mechanism for the formation of Pt skin may vary as the behavior of surface atoms change under different heat treatments in the atomic ordering step. Aberration-corrected environmental TEM was used to examine the surface evolution of Pt-Co bimetallic NPs during oxidation in O_2 and reduction in H_2 processes.[31] Under oxidation conditions, Co atoms could migrate to the surface to form a strained oxide layer. The surface strain was relaxed through the formation of Co oxide islands afterwards. The Co atoms could move back to the core during the reduction, resulting in the formation of Pt monolayer on the surface.

In another case, when atomic ordering of Pt_3Co NPs took place in O_2, $L1_2$-Pt_3Co intermetallic formed, together with the Pt surface segregation during the disorder-to-order transition (**Figure 8a-b**).[29] In that particular HR-STEM study, the false color image shows the atomic structures of {100} surface (**Figure 8a**, red box region). Two atomic layers of

Pt, instead of a monolayer, were observed on the {100} surface (**Figure 8b**). Such surface segregation of Pt effectively prevents the oxidation of Co. When temperature was decreased to 300 ° C, Pt atoms from other clusters migrated and attached on {100} facet of the $L1_2$-Pt_3Co NPs, giving rise to a layer-by-layer growth of Pt shell in the atmosphere of oxygen (**Figure 8c**).

Acid treatment could result in the formation of Pt shell with more than two atomic layers on intermetallic core (**Figure 8d and e**).[30] The fully ordered $L1_0$-PtCo NPs could form such core-shell structures after they were treated in 0.1 M $HClO_4$ at 60 ° C in air for 24 h, followed by annealing under 5% H_2 in Ar at 400 ° C for 2 h. STEM micrograph shows that the core-shell structure was formed with the core consisting of alternative layers of Pt and Co and the shell being 2~3 atomic thick of Pt. Such core-shell structure is efficient in protecting Co against acid etching.

Besides the above case studies where Pt atom was used, carbon[76, 93] and ionic liquids[106] were also used to make the shell. For example, dopamine was used to coat the carbon-supported Pt NPs and subsequently converted into nitrogen-doped carbon shell via pyrolysis under H_2 atmosphere.[93] Interestingly, even if Pt atoms were covered, enhanced catalyst durability was observed with a high ORR mass activity of 1.36 mA mg^{-1}_{Pt}.

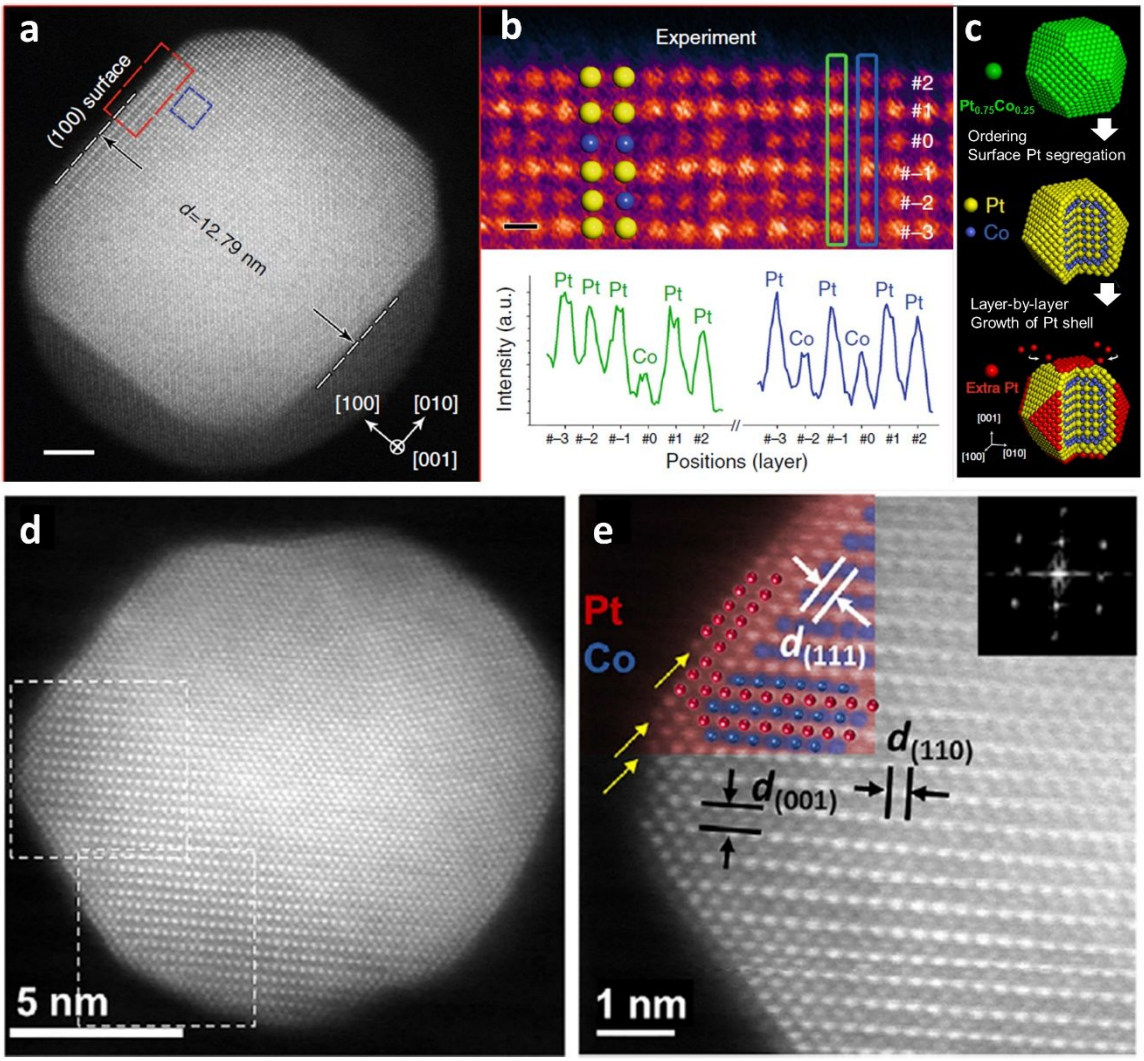

Figure 8. (a) *In-situ* HAADF-STEM image showing a Pt_3Co NP after being exposed to oxygen for 30 min at 720 ° C (scale bar: 2 nm). (b) Enlarged false color image of (100) surface in the red box in (a), and the intensity profiles taken along the atomic layers marked by green and blue rectangles, showing the segregated Pt-rich surface (scale bar: 2 Å). (c) Schematic diagrams showing the process of the oxygen-driven formation of core-shell structure in Pt_3Co NPs. Reproduced with permission from ref. 29. Copyright 2017, Nature Publishing Group. (d) STEM image of $L1_0$-PtCo/Pt NPs with 2-3 atomic layers of Pt shell on $L1_0$-PtCo core (dark atom is Pt and light atom is Co), zone axis is <1-10> direction. (e) Enlarged section indicated by the top dashed square in (d), showing the 2-3 atomic layers of Pt shell (indicated by yellow arrows) and the $L1_0$-PtCo core (red-Pt, blue-Co). Reproduced with permission from ref. 30. Copyright 2019, Cell Press.

4. Selective recent examples for the preparation of Pt-Co intermetallic NPs

Platinum-cobalt alloy NPs or their metal ions on catalyst support are usually needed to make intermetallic structure through heat treatment, because this approach greatly reduces atomic diffusion length for the formation of intermetallic. Furthermore, a low-temperature atomic ordering process is preferable to reduce the possibility of particle sintering and coalescence. There are two main steps in a typical synthesis of intermetallic NPs: preparation of alloys or metal ion intermediates as precursors, and conversion to intermetallic through atomic ordering. The second step is normally conducted using heat treatment in reductive gas atmosphere, and a microwave-induced ordering is also reported.[107] In this feature article, we categorize current methods for the synthesis of Pt-Co intermetallic NPs based on the initial step and summarize them in **Table 1**.

Colloidal synthesis is a popular method for preparing faceted, metal alloy NPs because the added surfactants can be adsorbed on certain metal facets (*i.e.*, {*hkl*}), and often slow down the growth rate in the corresponding [*hkl*] direction. Such solution phase synthesis has the advantage of easy control over the structure parameters of formed NPs.[108] The surfactants used may be adsorbed on crystal surfaces and block the catalytic active sites, although they can be removed during the heat treatment. For example, in the preparation of carbon-supported $L1_0$-PtCo NPs, PtCo alloy NPs were firstly prepared using $Pt(acac)_2$, $Co(acac)_2$, and OAm via colloidal synthesis.[30] OAm served as both the solvent and the reducing agent. The as-prepared alloy NPs were subsequently dispersed on carbon to prepare the intermetallic after being treated in $5\%H_2$ at 650 ° C for 6 h.

Impregnation is a common method for preparing Pt-Co intermetallic NPs. In this approach, metal precursors dissolve in aqueous or organic solvents and are loaded subsequently onto supports, typically made of various types of carbon. The optimal volume of the solvents is around the pore volume of the support, so capillary force may draw solution into the pores, resulting in uniform dispersion of metal precursors. Drying process, either by heat or freeze drying, is then carried out to remove the solvent. The solid products go through atomic ordering to produce intermetallic NPs. The metal precursors may be reduced directly to

intermetallic compounds, or form alloys first and then go through disorder-to-order transition.[59] Sometimes it takes more than one heating step to obtain the final products.[91] The detailed changes of the atomic restructuring process remain a difficult subject to study because of the limitation of *in-situ* characterization. Vulcan XC-72 and Ketjen black are the commonly used carbon supports. Mesoporous functionalized carbon made from pyrolysis of zeolitic imidazolate framework (*e.g.*, ZIF-8 and ZIF-67) was also reported.[78, 94, 109] Certain ZIF-derived carbon may function as the host structure for Co due to its atomically dispersive capability of metal species.[110] Heteroatoms are often incorporated into the carbons support and help to enhance support-metal interaction, thus achieving a better size control.[90, 91]

Co-reduction is used to produce Pt and Co metal species, or more specifically Pt-Co alloys, from the corresponding salt precursors in liquid phase. In this case, reducing agents such as sodium borohydride ($NaBH_4$) is required.[99, 111] For example, Co could be introduced first through the reduction of its salt by $NaBH_4$ in aqueous solution. A mixture of K_2PtCl_6 and $HAuCl_4$ was then added to the aqueous solution and sonicated to obtain AuPtCo alloy core-shell NPs.[111] After the atomic ordering via heat treatment, $L1_0$-$Au_{10}Pt_{40}Co_{50}$ core-shell half-intermetallic NPs formed.

Surface coating and template-assisted syntheses are often conducted to produce specific nanostructures. Dopamine was applied as surface coating molecule to synthesize $L1_0$-PtCo intermetallic NPs with a nitrogen-doped carbon shell that protects $L1_0$-PtCo from metal leaching in the electrochemical processes.[93] Dopamine was also used to form a polymeric surface around NPs against particle growth in the heat treatment steps.[92] As for template-assisted synthesis, template is used to either produce intermetallic with controlled morphology[99] or control the structure of carbon support.[112]

Table 1. Synthesis procedures of selected Pt-Co intermetallic nanostructures.

Colloidal synthesis					
Composition	**Intermetallic structure**	**Precursor**	**Support (spec), additive**	**Processing condition for ordered phase**	**Ref**
W-doped PtCo	$L1_0$	$Pt(acac)_2$, $Co(acac)_2$	carbon (Vulcan XC-72), OAc, OAm	400 °C, 1 h (5%H_2/Ar)	80

PtCo	$L1_0$	$Pt(acac)_2$, $Co(acac)_2$,	carbon (Vulcan XC-72), OAm, $W(CO)_6$,	600 °C, 4 h (4%H_2/Ar)	97
PtCo	$L1_0$	$Pt(acac)_2$, $Co(acac)_2$,	carbon (Ketjen-300J), OAm	650 °C, 6 h (5%H_2/Ar)	30

Impregnation-based synthesis

Composition	Intermetallic structure	Precursor	Support (spec)	Processing condition for ordered phase	Ref
PtCo	$L1_2$	H_2PtCl_6, $CoCl_2$	carbon (Vulcan XC-72)	650 °C, 4 h (10%H_2/N_2)	95
PtCo	$L1_0$	H_2PtCl_6, $C_{16}H_{40}Cl_4CoN_2$	carbon (N-doped)	700 °C, 1 h (vacuum)	59
PtCo	$L1_0$	H_2PtCl_6, $Co(NO_3)_2$	carbon (N-doped)	700 °C, 2 h (H_2/N_2)	88
$PtCo_{1-x}Ni_x$	$L1_0$	H_2PtCl_6, $CoCl_2$, $NiCl_2$	carbon (Vulcan XC-72)	700 °C, 2 h (H_2)	77
Pt_3Co	$L1_2$	H_2PtCl_6, $CoCl_2$	carbon (Vulcan XC-72)	700 °C, 2 h (H_2)	28
$PtCo_{1-x}Cu_x$	$L1_0$	H_2PtCl_6, $CoCl_2$, $Cu(NO_3)_2$	carbon (EC-300J)	700 °C, 2 h (5%H_2/Ar)	81
N-doped Pt_3Co	$L1_2$	H_2PtCl_6, $CoCl_2$	carbon (Vulcan XC-72)	700 °C, 2 h (NH_3)	113
Pt_3Co	$L1_2$	H_2PtCl_6, $CoCl_2$	carbonized ZIF-8	750 °C, 2 h (8%H_2/Ar)	94
$Pt_3Co_{0.6}Ti_{0.4}$	$L1_2$	H_2PtCl_6, $CoCl_2$, $TiCl_3$	carbonized ZIF-8	750 °C, 2 h (H_2/Ar)	78
PtCo	$L1_0$	H_2PtCl_6, $CoCl_2$	carbon (Ketjen black)	800 °C, 2 h (5%H_2/Ar)	33
Pt_3Co	$L1_2$	H_2PtCl_6, $CoCl_2$	carbon (Ketjen black)	800 °C, 2 h (5%H_2/Ar)	33
PtCo	$L1_0$	H_2PtCl_6,	bimetallic MOF Zn_xCo_y-derived carbon materials	900 °C, 2 h (5%H_2/Ar)	109
PtCo	$L1_0$	H_2PtCl_6, $CoCl_2$	carbon black	900 °C, 2 h (H_2), followed by 600 °C, 6 h (H_2)	91
Pt_3Co	$L1_2$	H_2PtCl_6, $Co(NO_3)_2$	carbon (S-doped)	950 °C, 2 h (5%H_2/Ar), followed by 600 °C, 6 h (5%H_2/Ar)	90

Co-reduction

Composition	Intermetallic structure	Precursor	Support (spec), reductant	Processing condition for ordered phase	Ref
Pt_3Co	$L1_2$	H_2PtCl_6, $CoCl_2$	carbon (Vulcan XC-72), $NaBH_4$	600 °C, 2 h (H_2)	99
$Au_{10}Pt_{40}Co_{50}$	$L1_0$	K_2PtCl_4, $HAuCl_4$, $Co(HCOO)_2$	carbon (Vulcan XC-72), $NaBH_4$	700 or 800 °C, 0.5 h (H_2/Ar)	111

Surface coating					
Composition	**Intermetallic structure**	**Precursor**	**Additive**	**Processing condition for ordered phase**	**Ref**
PtCo	$L1_0$	Pt/C, $Co(NO_3)_2$	dopamine, tetraethyl orthosilicate	800 °C, 2 h (10%H_2/N_2)	93
Pt_3Co	$L1_2$	H_2PtCl_6, CoCl2	polydopamine, carbon (Vulcan XC-72)	900 °C, 0.5 h (Ar)	92
Template-assisted synthesis					
Composition	**Intermetallic structure**	**Precursor**	**Template**	**Processing condition for ordered phase**	**Ref**
Pt_3Co	$L1_2$	H_2PtCl_6, $CoCl_2$	silica (SBA-15)	600 ° C, 2 h (H_2)	99
PtCo	$L1_0$	H_2PtCl_6, $CoCl_2$	polystyrene	700 °C, 2 h (H_2/Ar)	76
Pt_3Co	$L1_2$	H_2PtCl_6, $Co(NO_3)_2$	NaCl, glucose	790 °C, 2 h (5%H_2/Ar)	112
Other methods					
Composition	**Intermetallic structure**	**Precursor**	**Additive**	**Processing condition for ordered phase**	**Ref**
PtCo	$L1_2$	K_2PtCl_4, $Co(NO_3)_2$, 2-methylimidazole	-	600 °C, 3 h (5%H_2/Ar)	114
PtCo	$L1_0$	$Co(CH_3COO)_2$, K_2PtCl_4	carbon (Ketjen black) or carbon (Vulcan XC-72)	600 °C, 24 h (Ar)	115
$PtCo_3$	$L1_2$	H_2PtCl_6, $Co(NO_3)_2$	polyvinyl pyrrolidone, carbon (Vulcan XC-72)	600 or 700 °C, 2 h (H_2)	55
PtCo	$L1_0$	H_2PtCl_6, $CoCl_2$	ionic liquid, carbon black	700 °C, 2 h (N_2)	106
Pt_3Co	$L1_2$	H_2PtCl_6, $CoCl_2$	carbon (Vulcan XC-72)	700 °C, 2 h (H_2/N_2)	102
PtCo	$L1_0$	H_2PtCl_6, $Co(NO_3)_2$	$NH_3 \cdot H_2O$, carbon (Vulcan XC-72)	700 °C, 2.5 h (10%H_2/Ar)	104
PtCo	$L1_0$	K_2PtCl_4, $K_3Co(CN)_6$,	-	700 °C, 68 h (Ar)	116
Pt_3Co	$L1_2$	K_2PtCl_4, $K_3Co(CN)_6$, $CoCl_2$	-	750 °C, 2 h (Ar)	116
Pt_3Co	$L1_2$	H_2PtCl_6,	Co-doped ZIF derived carbon	900 °C, 0.5 h (vacuum)	110
Cu-doped PtCo	$L1_0$	$Pt(acac)_2$, $Cu(acac)_2$, $Co_2(CO)_8$	carbon (Vulcan XC-72)	microwave, 1200 W, 30 s, (5%H_2/N_2)	107

In general, there is a tradeoff in the synthesis of Pt-Co intermetallic NPs for the optimal electrocatalytic performance. The choice of temperature and heating profile are often crucial for producing intermetallic structure. High temperature is beneficial to facilitates atomic diffusion and increase crystallinity, though it may result in an increase in both size and size distribution, because both particle sintering and Ostwald ripening may occur under such processing condition. Inversely, low temperature process may be good for size control, but suffer from low degree of ordering. In addition, surfactants and excess surface carbon may not be removed at low synthesis temperatures. Similarly, the incorporation of protective layer such as carbon shells needs to balance between size control and deactivation or blocking of surficial active sites. The enhanced support-metal interaction is effective in inhibiting atomic diffusion and particle migration in the disorder-to-order transition, though the energy barrier for atomic ordering may increase. The loading amount of metal precursors should be controlled. Low loading is preferred for highly uniform dispersion of intermetallic NPs, but it increases the average atomic diffusion length during ordering process and reduces the packing density of the catalyst NPs. Thus, controlled experiments and optimization are necessary to scrutinize the effect of different conditions for the preparation of highly ordered, size-controlled Pt-Co intermetallic NPs.

5. Application of Pt-Co intermetallic NPs in electrocatalysis

Many Pt-M (M=Co, Fe, Ni) bimetallic materials are theoretically predicted to possess better ORR activity than pure Pt NPs.[9, 26, 27, 117] However, electrocatalysts consisting of Pt-Fe species suffer from Fenton reaction, of which ferrous and ferric cations can catalyze the formation of oxidizing agents from H_2O_2, accelerating the degradation of electrocatalysts or decomposition of fuel cell components (*e.g.*, Nafion membrane). Electrocatalysts made from Pt-Ni alloys may exhibit high ORR activity,[18, 118, 119] though they may be harder to synthesize and less stable than Pt-Co. In this context, electrocatalysts consisting of Pt-Co alloy NPs attract much attention, especially after its use in commercial fuel cell systems.[40] With the need for heavy-duty applications,[13] addressing the challenge in durability becomes increasingly critical.

Pt-based intermetallic NPs, in this regard, have better stability than their alloy counterparts.[105, 120-122] The ORR stability may be attributed to the strong bonding between Pt and the other metal, which results in a more negative enthalpy of formation.[43, 44] Intermetallic often exhibits less metal dissolution, less ECSA loss, and better durability than its alloy form under the same running conditions.[123, 124] Furthermore, there is an ease in analyzing the composition of near-surface region of intermetallic structures,[43, 96] which help to develop more reliable surface models in theoretical calculation of adsorption[111, 125, 126] and mechanism study of a catalyst.[78, 80, 117] In this section, we discuss the correlation between structural features and catalytic properties of Pt-Co intermetallic electrocatalysts, *i.e.*, activity and durability.

Briefly, there are two major experimental approaches to the characterization of electrocatalysts: the three-electrode system based on rotating disk electrode (RDE) technique and the full cell study using membrane electrode assembly (MEA). The RDE test is primarily based on the analysis of polarization curve obtained from linear scanning voltammetry (LSV). The value of current density under different potential (*vs.* reversible hydrogen electrode, RHE) is frequently used to compare the performance in the kinetically controlled regime, because RDE technique can greatly reduce the effect of mass transport. Mass activity in A/mg_{Pt} obtained from the polarization curve at 0.9 V (*vs.* RHE) is a common parameter for comparing the ORR activity. When other precious metal (*e.g.*, Pd) is incorporated, mass of all noble metals should be included besides Pt, in part because of the economic consideration of the scale-up production of PEMFCs. Area specific activity (or specific activity) is used to compare the intrinsic activity based on electroactive metal site. In the latter case, the value of surface area is obtained based on ECSA measurement, which is an estimation of Pt (or Pd) metal sites calculated based on {111} surface and should be distinguished from the geometric surface area. On durability, accelerated stress test (AST) is a primary testing method whereas an applied potential continuously cycles in the predetermined potential window. Mass activity is reported at the beginning of life (BOL) and the end of life (EOL, usually 30k cycles). The percentage retention of mass activity quantitatively describes durability. **Table 2** summarizes the RDE-based ORR performance data of Pt-Co intermetallic electrocatalysts reported in recent years, based on the activity and durability metrics.

Table 2. Summary of ORR catalytic performance before and after AST for selected Pt-Co intermetallic catalysts based on RDE measurement.

Catalyst			Mass activity @ 0.9 V (A/mg_{Pt})		Durability (%) (test condition)	Ref
Name	Core@shell	Intermetallic structure	BOL	EOL		
PtCo@Pt	Pt-shell	$L1_0$	0.48	0.38	80 (60k, 0.6~1.0 V)	109
O-$PtCo_3$@HNCS	carbon shell	$L1_0$	0.54	0.50	92.6 (20k, 0.6~1.0 V)	76
$L1_0$-PtCo/C	-	$L1_0$	0.67	0.64	96.7 (10k, 0.6~1.0V)	59
AuPtCo/C-700	Pt shell	$L1_0$	0.68	0.66	97.1 (10k, 0.6~1.0 V)	111
PtCo/C-600	Pt shell	$L1_2$	0.68	0.51	74.9 (30k, 0.6~1.0 V)	95
Pt-Co-Mo	Pt shell	$L1_0$	0.89	0.62	70 (30k, 0.6~1.0 V)	126
fct-PtCo/C@ILs	ionic liquid shell	$L1_0$	1.04	0.94	90.4 (10k, 0.6~1.1 V)	106
$L1_0$-PtCo	-	$L1_0$	1.27	0.80	63 (30k, 0.6~1.1 V)	88
PtCo@NC-60	carbon shell	$L1_0$	1.36	1.26	93 (20k, 0.6~1.2 V)	93
$Pt_3Co_{0.6}Ti_{0.4}$	Pt-shell	$L1_2$	1.49	1.19	79.9 (20k, 0.6~1.05 V)	78
$L1_0$-W-PtCo/C	Pt shell	$L1_0$	2.21	2.04	92.3 (10k, 0.6~1.0 V)	80
$L1_0$-CoPt	Pt shell	$L1_0$	2.26	1.83	81.0 (30k, 0.6~1.0 V)	30
fct-Pt-Co@Pt/C	Pt shell	$L1_0$	2.82	2.23	79.1 (30k, 0.6~1.1 V)	97
$L1_0$-CoNiPt	Pt shell	$L1_0$	3.1	2.6	84 (30k, 0.6~1.0 V)	117

***** The value of durability is the retention of mass activity at 0.9 V (*vs.* RHE), which is obtained or estimated from the reported polarization curves. Numbers in the parentheses represent the numbers of AST cycles and the corresponding potential window. Only intermetallic catalysts with no less than 10k AST cycles are listed in Table 2. The values of EOL mass activities in Table 2 are calculated based on reported BOL mass activities and retention rates if they are not explicated reported in the referred publications.

Noticeably, RDE-based measurements focus on optimizing the testing conditions to reduce the mass transfer resistance and other factors for obtaining the highest kinetic current density data. As the catalytic test takes place in liquid using RDE technique while the MEA-based single cell study operates under different levels of humidity, ORR performance data cannot be compared directly between these two types of measurements.[88,

[104] The discrepancy between RDE and MEA results is often quite large and can be attributed to multiple factors. Mass transfer resistance is often much higher in MEA test than in the RDE-based measurement. In addition, the MEA tests are usually performed under high metal loading, elevated temperature, and with different backpressure and humidity, using both air and pure oxygen in MEA stack.[127] All of these conditions affect the catalytic performance. In addition, leaching of non-Pt metal could corrode the MEA. In this context, MEA measurement becomes increasingly important, especially in the development of PtCo-based NP electrocatalysts designed for durable PEMFC systems towards heavy-duty applications.

The typical MEA-based assessments of catalytic performance share a few common features with those of RDE tests. In a widely used AST protocol, mass activity at the cell voltage of 0.9 V is measured before and after 30,000 times of square wave cycles between 0.6 and 0.95 V. While there exist other electrochemical stability test protocols such as pulse cycling methods, the aforementioned AST method can simulate the material degradation in the MEA under the operating conditions over a much shorter time frame than the rest.[38] The potential loss at 0.8 A/cm^2 is important for the AST, and reported from the polarization curves after predetermined numbers of cycles (*i.e.*, 1k, 5k, 10k, 30k), together with the percentage loss in ECSA.[37] There are fewer reports on MEA-based ORR performance of Pt-Co intermetallic electrocatalysts because of multiple reasons, which include difficulty in preparing high-quality MEA reproducibly, uncontrollable variation in the testing conditions, and differences in testing protocol. **Table 3** summarizes a selection of recently reported MEA results using the suggested metrics in order to compare the results under the same or comparable conditions.

Table 3. Summary of ORR catalytic performance for state-of-art Pt-Co intermetallic catalysts based on the MEA measurement.

Gas type	Catalyst	Mass activity @ 0.9 V (cell voltage)			Loss in potential (mV) (@ a given current density in A/cm^2)	Loss in ECSA (%) (number of AST cycles)	Ref
		BOL (A/mg$_{Pt}$)	EOL (A/mg$_{Pt}$)	Retention (%)			
H_2-O_2	$L1_0$-CoPt	0.56	0.45	81	-	12.9 (30k)	30
	$L1_0$-W-PtCo/C	0.57	0.47	82.5	-	-	80
	$L1_0$-CoPt@Pt-shell	0.60	0.36	60	-	-	122
	Sub-Pt_3Co-MC	0.92	0.81	87.8	-	-	33
	PtCo i-NPs	1.52	1.17	77	-	-	90
H_2-air	Pt_3Co/C-750	0.5	0.4	80	20 (2)	27 (30k)	61
	PtCo/KB-NH_2	0.691	0.380	55.0	30 (0.8)	-	128
	Pt_3Co/FeN_4-C	0.72	0.441	38	23 (1.0) 21 (0.8)	-	125
	STG-assisted PtCo	1.08	0.81	75	21 (0.8)	-	91
	Pt_3Co/DMC-F	-	-	-	-	20.9 (10k) 30 (20k)	94
	$Pt_3Co_{0.6}Ti_{0.4}$	-	-	-	-	19.8 (30k)	78
	$L1_0$-CoPt@Pt-shell	-	-	-	26 (0.8)	33 (30k)	122

The degree of ordering of the intermetallic Pt-Co electrocatalyst was found to correlate well with the ORR activity[60, 71, 84, 85, 129] and a higher degree of ordering results in higher activity.[61] Incorporation of a third metal into the Pt-Co intermetallic system (*i.e.*, mixed-element half-intermetallic) helped change the Pt-Pt distance to optimize the binding energy between Pt and O intermediates on the surface.[78, 80, 81] Surface of $L1_0$-PtCo NPs modified by Mo-O_x species (**Figure 9a and b**) could exhibit a weakened binding energy of oxygen species on Pt (**Figure 9c and d**), resulting in an enhancement in ORR performance under both RDE and MEA testing conditions.[126] Single atoms of Co-N-C support may change the binding energy between oxygen species and Pt surface, whereas the direct electron transfer from PtCo to Co-N-C support could result in *d*-band shift of Pt.[130, 131]

The incorporation of metal into the Pt-Co lattice may change the surface strain and enhance the ORR activity.[117] An eigenforce model was constructed to predict the strain-induced enhancement of ORR activity (**Figure 9e**). This model was used to analyze the

ORR performance based on the two popular mechanisms: the associative, in which the O-O bond stays intact upon adsorption and protonation (**Figure 9f**), and the dissociative, in which the O-O bond is broken upon adsorption (**Figure 9g**). The underlying principle is that change on a subdomain of an extended surface may result in eigenstress on the surface boundary. The adsorbed oxygen species may cause either the attraction or repulsion of the neighboring metal atoms. Understanding the interplay between applied strain and the induced eigenstress helps to predict the effect of strain on the binding of adsorbates. A 2D volcano plot could be created to locate the optimal ternary NPs, by calculating binding energy of Pt surfaces of different $L1_0$-$PtCo_{0.5}M_{0.5}$ (M=Mn, Fe, Ni, Cu, Ni) (**Figure 9f and g**). This theoretical screening guided the synthesis of $L1_0$-PtCoNi NP electrocatalyst, which exhibited a mass activity of 3.1 A/mg_{Pt} and a specific activity of 9.3 mA/cm^2 at 0.9 V (*vs.* RHE). The RDE-based AST showed a 15.9% loss of mass activity after 30k cycles at 60 °C in 0.1 M $HClO_4$.

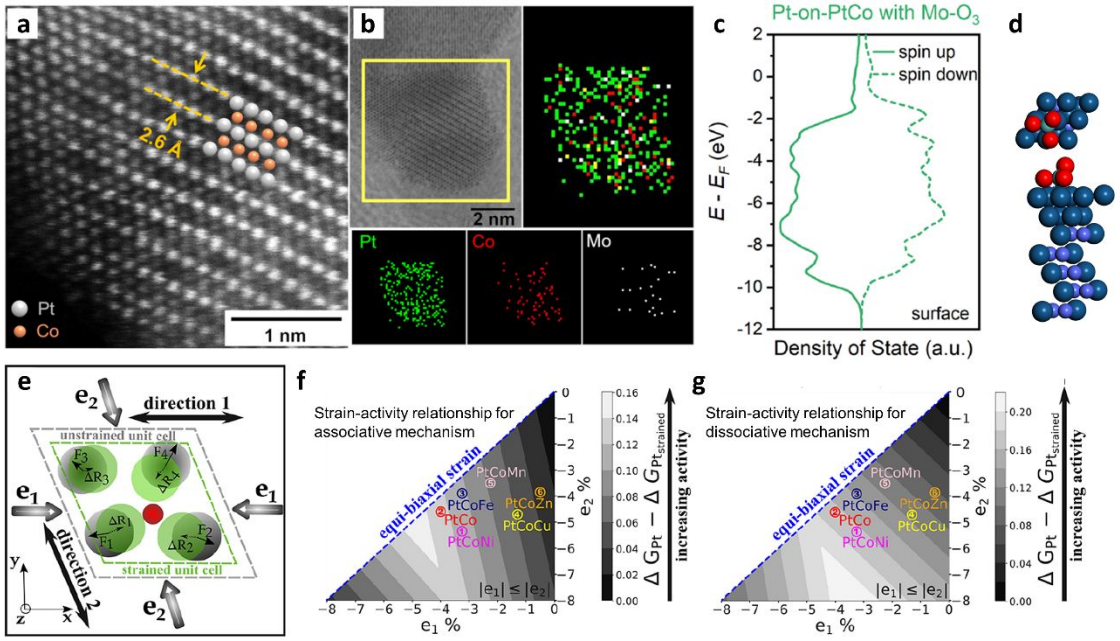

Figure 9. (a) High-resolution HAADF-STEM micrograph showing the intermetallic features of the Pt-Co-Mo electrocatalyst. (b) HAADF-STEM EDS map showing the Pt, Co, Mo distribution of the catalyst particle in (a). (c) Calculated density of states of the *d*-orbitals of the surface Pt, and (d) top/side view of Pt-on-PtCo with Mo-O_3 structures. Reproduced with permission from ref. 126. Copyright 2022, Elsevier. (e) Illustration of the

in-plane components of the adsorbate-induced eigenforces and the displacement caused by an applied strain. Calculated 2D volcano plots of strained Pt {111} surfaces using the eigenforce model for (f) the associative mechanism, and (g) the dissociative mechanism. Reproduced with permission from ref. 117. Copyright 2020, American Chemical Society.

Size control plays an important role in improving the ORR activity of PtCo intermetallic electrocatalysts.[33, 59, 88, 90, 94] **Figure 9** shows the ORR activity and durability studies of sub-3 nm $L1_0$-PtCo NPs supported on nitrogen-doped carbon.[59] The strong electrostatic adsorption of metal species on functionalized carbon helped in suppressing the particle sintering during the heat treatment. Such PtCo intermetallic electrocatalyst exhibited a half-wave potential 64 mV higher than that of the Pt/C (**Figure 10a**). Both the mass and specific activities of intermetallic PtCo electrocatalysts were significantly higher than Pt/C and *fcc* PtCo random alloy phase in RDE tests (**Figure 10b**). Moreover, the PtCo intermetallic electrocatalyst, which had the highest activity among the three, exhibited only a 3.3% drop in the mass activity after 10k of RDE-based AST cycles. The mass activity dropped by 30% for the PtCo random alloy catalyst tested under the same conditions (**Figure 10c**). Such study demonstrates the advantages in both activity and durability of using PtCo intermetallic NPs as ORR electrocatalysts.

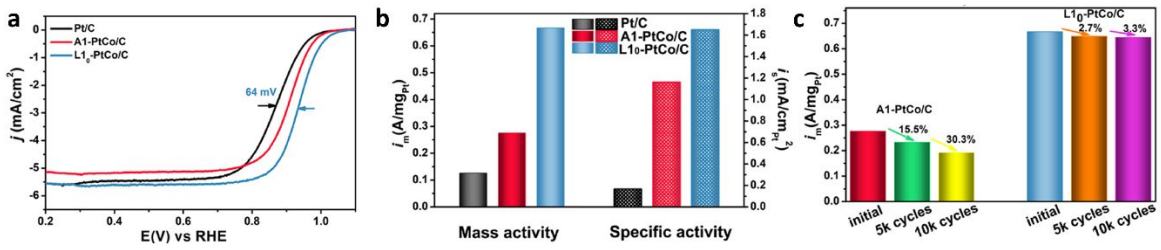

Figure 10. (a) ORR polarization curves, (b) mass- and area-specific activities at 0.9 V (*vs.* RHE), and (c) mass activity for the initial, 5k, and 10k CV cycles for the sub-3 nm ordered, intermetallic $L1_0$-phase PtCo/C electrocatalysts, respectively. Reproduced with permission from ref. 59. Copyright 2021, Elsevier.

The shape of Pt-Co intermetallic NPs can be an important structural factor for the ORR performance, since lattice mismatch between intermetallic core and the Pt shell[101] results in different levels of induced strain based on the exposed surfaces.[109, 132] Such strain effect and ligand effect were studied by theoretical calculations.[99, 117] Subsize $L1_2$-Pt_3Co NPs with

2~3 atomic thickness Pt skin exhibited enhanced activity.[33] The *d*-spacing of Pt {111} skin in this core-shell intermetallic structure is 0.09 Å smaller than that of pure Pt. Such contraction resulted in an increased overlap of the 5*d* electron cloud of surface Pt sites and caused downward shift of the antibonding states of O-Pt. This weaker binding energy of oxygen intermediates could lead to the high intrinsic ORR activity.

Enhancement in activity was reported for $L1_0$-PtCo intermetallic nanowires with high-index facets.[22] The $L1_0$-PtCo nanowire electrocatalyst had a high ratio of {221} facets and exhibited a mass activity of 1.30 A/mg_{Pt} at 0.9 V (*vs.* RHE). Theoretical calculations suggested that the {111} terraces of the {221} facets are strained by both the presence of sub-surface Co and the nature of high-index facet, resulting in high ORR activity on the *fcc* hollow (active) sites. The {111} terraces also extended enough to avoid deactivation by interacting with the oxygen species on the step sites.

Multiple structural factors may work synergistically to affect the observed ORR activity. Electrocatalysts made of octahedral $L1_0$-PtCo NPs with ultrathin Pt shell had a mass activity of 2.82 A/mg_{Pt} at 0.9 V (*vs.* RHE), which is 13 times of the commercial Pt/C catalyst.[97] The authors attributed this large enhancement to three possible reasons. First, the ordered intermetallic structure resulted in strong ligand and stain effects in near-surface regions.[96] Second, the exposure of Pt {111} facets in the octahedral shape exhibited anisotropic strains. Third, the active sites on surfaces were fully exposed.

Similarly, multiple structural factors help to enhance the durability of Pt-Co intermetallic electrocatalysts, which include the degree of ordering,[83, 122] composition,[111, 130, 133] particle size,[33, 83, 94] and core-shell structure.[28, 30, 93, 100] The impact of structural ordering of Pt-Co catalyst on metal (Pt and Co) dissolution and re-deposition, as well as the associated durability under PEMFC operational conditions was revealed by microscopic study.[83] Since the oxidation of surface Pt atoms is often the cause for the dissolution of Pt-based NP electrocatalysts, eliminating the reactive corner and edge sites of $L1_0$-PtCo NPs by addition of a less reactive metal such as Au could improve durability through blocking the oxidation of Pt at these sites.[111, 133] The Au-incorporated $L1_0$-PtCo intermetallic electrocatalyst exhibited an initial mass activity of 0.67 A/mg_{Pt} and ended with a value of 0.64 A/mg_{Pt} after 10k RDE-based AST cycles, showing a 97% retention.[111]

There are various reports on the effects of PtCo particle size on ORR durability. Subsize Pt-Co intermetallic NPs was found to enhance the stability of the membrane electrode through preventing the poisoning by ionomers in humid fuel cells.[33] At the BOL of MEA test, $L1_2$-Pt_3Co electrocatalyst exhibited a mass activity of 0.92 A/mg_{Pt} at 0.9 V (cell voltage), which is six times that of commercial Pt/C. The mass activity reduced to 0.84 A/mg_{Pt} (8.7% loss) after 10k cycles and 0.75 A/mg_{Pt} (18.5 % loss) after 30k cycles in the MEA-based test. The confinement of mesoporous carbon was reported to not only control the particle size of $L1_2$-Pt_3Co NPs but also mitigate their aggregation during the electrochemical reactions and significantly suppress the detachment of catalyst particles.[94] The as-made electrocatalysts showed 13.3% loss in mass activity after the RDE-based AST. The MEA made from the same catalyst underwent a 15.4% decrease in current density at 0.6 V (cell voltage) after 20k cycles, which was less than that of the commercial Pt/C MEA after 10k cycles (15.8% loss). The $L1_0$-PtCo electrocatalyst may retain 77% of its initial mass activity after 30k AST cycles in MEA if they were anchored strongly on the support through enhanced support-metal interaction. The intermetallic core-shell structure of this catalyst was preserved after the AST, suggesting the structural stability.[90]

In addition, optimized core-shell structure could also contribute to the ORR durability of PtCo intermetallic electrocatalysts.[28, 100] Nine nanometer-sized, hard-magnet $L1_0$-PtCo NPs with 2~3 atomic layer Pt shell were prepared as the electrocatalysts.[30] In RDE tests, the catalysts exhibited a BOL mass activity of 2.26 A/mg_{Pt}, which was 19 times of the commercial Pt/C. The mass activity was 1.88 A/mg_{Pt} after 20k AST cycles and 1.83 A/mg_{Pt} after 30k AST cycles. In the MEA tests, the catalysts achieved a mass activity of 0.56 A/mg_{Pt} at the BOL and 0.45 A/mg_{Pt} after 30k AST cycles. Theoretical calculations attributed the enhanced ORR performance to the biaxial strain induced by the Pt shell. Carbon shell may serve as a protective layer to improve durability if it is designed in such a way that does not block active sites of the electrocatalyst.[93] For electrocatalysts consisting of $L1_0$-PtCo NPs with nitrogen-doped carbon shell, its mass activity retained a high value of 1.36 A/mg_{Pt} after 20k AST cycles in RDE-based tests. This performance value represents a loss of only 7% in activity.

Enhanced durability of Pt-Co intermetallic in MEA was achieved through the control of both size control and carbon shell.[91] A small-molecule-assisted impregnation approach was used to synthesize various intermetallic NPs. Small molecules such as sodium thioglycolate (STG) was added to the metal precursors and sulfur-doped carbon shell coating the intermetallic NPs formed after annealing. Such carbon coating successfully suppressed particle sintering and insured formation of ultrafine intermetallic NPs (**Figure 11a-c**). In H_2-O_2 single-cell test, the STG-assisted $L1_0$-PtCo catalyst exhibited a high mass activity of 1.08 A/mg_{Pt} at 0.9 V, which exceeded the US DOE 2025 target of 0.44 A/mg_{Pt} (**Figure 11d**). The mass activity decreased by 25% after 30k AST cycles in MEA. The STG-assisted $L1_0$-PtCo catalyst was tested in a H_2-air single cell at 80 ° C, 100% relative humidity (RH), and 150 kPa_{abs}. The current density of the cell was 412 mA/cm^2 at 0.8 V and exceeded the DOE 2025 target of 300 mA/cm^2 (**Figure 11e**). After 30k AST cycles, the voltage loss of STG-assisted $L1_0$-PtCo catalyst at 0.8 mA/cm^2 was 21 mV, which is below the DOE 2025 target of 30 mV loss at maximum (**Figure 11f**). Noticeably, there is a large discrepancy between RDE- and MEA-based results. Further effort is required to enhance the durability of Pt-Co intermetallic electrocatalysts in MEA for practical applications. In addition, it should be noted that besides ORR in this article, Pt-Co intermetallic NPs have also been tested for CO oxidation,[134-138] alcohol oxidation,[56, 130] formic acid oxidation,[77] hydrogen evolution reaction,[22] and dehydrogenation.[75]

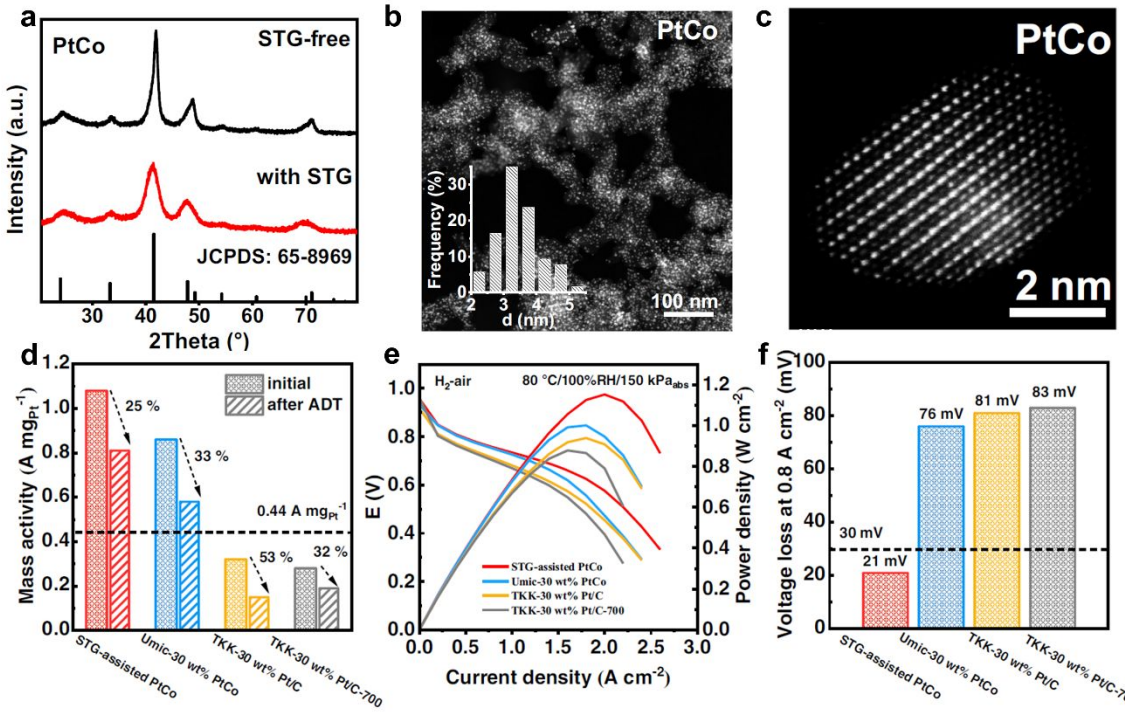

Figure 11. (a) XRD pattern, (b) HAADF-STEM image (inset: size distribution), and (c) atomic-resolution HAADF-STEM image of PtCo intermetallic NPs. (d) Mass activity loss of different cathode catalysts (STG-assisted PtCo, Umic-30 wt% PtCo, TKK-30 wt% Pt/C, and TKK-30 wt% Pt/C-700) after 30k cycles. (e) Polarization curves and power density plots in the H_2-air cell and (f) the voltage loss at 0.8 A cm^{-2}. All ORR properties were determined using MEA-based tests. Reproduced with permission from ref. 91. Copyright 2022, Nature Publishing Group.

6. Conclusions

In this feature article, we analyze the thermodynamic and kinetic factors governing the preparation of a variety of Pt-Co based intermetallic NPs. A key aspect to consider is the energy barrier for atomic ordering, which requires heat treatment, to produce PtCo intermetallic NPs. Advances in characterization methods enable both *in situ* and *ex situ* studies of the atomic ordering process at nanoscale, thus helps our understanding of the formation mechanism at the atomic level. Such studies are often the key for uncovering the principles on how to design Pt-Co intermetallic with different compositions, size, and shape. The need for producing highly active and durable ORR electrocatalyst drives the development of novel Pt-Co intermetallic with ever-complexing and finely controlled

nanostructures. The advantage of using Pt-Co intermetallic electrocatalysts is its durability improvement in PEMFCs.

Although there has been much progress on the Pt-Co intermetallic NP as ORR electrocatalysts in recent years, several challenges remain. Firstly, there is still a major need to develop the methodology for creating highly ordered intermetallic structures, as metal segregation and local inhomogeneity often exist in many of the current products of PtCo intermetallic NPs. In this context, careful examination of the degree of ordering is required in assessing the crystallinity of the intermetallic structure. The threshold values between alloy and intermetallic remain unclear. The best practice in analyzing the structure and catalytic performance of Pt-Co intermetallic NPs with different degree of ordering still needs to be developed. Local inhomogeneity requires accurate and non-destructive characterization methods to analyze the Pt/Co ratio and other key variables.[139] Secondly, for the disorder-to-order transition, there are constraints in the study of atomic ordering mechanism to only a few scenarios such as thermal annealing because of the limitation of *in-situ* characterization methods. Empirical studies are often the approaches to identifying the optimal conditions for atomic ordering. Thirdly, certain Pt-Co intermetallic phase, namely the $L1_2$-$PtCo_3$, is theoretically predicted, but there is a lack of experimental reports.[55-57] Thus, performance of Co-rich intermetallic remains largely unknown. Incorporation of a third metal into the Pt-Co intermetallic NPs raise new possibilities for versatile electrocatalysts. However, similarity between the third metal (*i.e.*, Fe, Ni, Cu, Ti, etc.) and Co atoms makes the microscopic characterization difficult, thus the structural details of these "half-intermetallic" are unclear. Fourthly, the morphologies of current Pt-Co intermetallic are mainly quasi-spherical and partially faceted. The synthesis and property studies of 1D, 2D, and higher-ordered (*i.e.*, hierarchical and porous structures) Pt-Co intermetallic NPs could be intriguing. Synthesis of low-dimensional or complex intermetallic nanostructures are closely related to the understanding of surface energy control of different facets. Fifthly, for Pt-Co intermetallic electrocatalyst, the MEA durability performance is still far from reaching the maximum or high-activity values demonstrated in the RDE studies. How to design such intermetallic ORR electrocatalysts for MEAs continue to be a challenge. In this context, there is a need to design low-cost testing strategies to understand the degradation mechanisms and effects of electrolytes and

operating conditions in a full cell study. While intermetallic Pt-Co nanoparticles are often good electrocatalysts for ORR with high durability, excess dissolution of Co atoms from $L1_2$ Pt_3Co intermetallic was observed and attributed to the lack of formation of Pt skin layer.[140] Thus, additional factors beyond the ordered intermetallic structures should be considered, especially for durability. Development in microscopic characterization methods in dynamic tracking and modeling, reliable prototyping in MEA testing, and bridging techniques to better utilize the RDE test for understanding full cell performances thus become increasingly important.[141]

Conflicts of interest

There are no conflicts to declare.

Acknowledgements

We would like to thank the U.S. National Science Foundation and our industrial sponsors for their past and current supports, and our colleagues in the Yang group whose work is presented in this feature article.

Notes and references

1. J. Carter, G. McVinker, W. Weissman, M. Kmak and J. Sinfelt, *Appl. Catal.*, 1982, **3**, 327-346.
2. M. Omrani, M. Goriaux, Y. Liu, S. Martinet, L. Jean-Soro and V. Ruban, *Environ. Pollut.*, 2020, **257**, 113477.
3. M. Jeyaraj, S. Gurunathan, M. Qasim, M.-H. Kang and J.-H. Kim, *Nanomaterials*, 2019, **9**, 1719.
4. J. Wu and H. Yang, *Acc. Chem. Res.*, 2013, **46**, 1848-1857.
5. Z. Peng and H. Yang, *Nano Today*, 2009, **4**, 143-164.
6. J. Peng, P. Tao, C. Song, W. Shang, T. Deng and J. Wu, *Chin. J. Catal.*, 2022, **43**, 47-58.
7. C. Wang and J. S. Spendelow, *Curr. Opin. Electrochem.*, 2021, **28**, 100715.
8. M. Zhou, C. Li and J. Fang, *Chem. Rev.*, 2021, **121**, 736-795.
9. J. Greeley, I. Stephens, A. Bondarenko, T. P. Johansson, H. A. Hansen, T. Jaramillo, J. Rossmeisl, I. Chorkendorff and J. K. Nørskov, *Nat. Chem.*, 2009, **1**, 552-556.
10. X. X. Wang, J. Sokolowski, H. Liu and G. Wu, *Chin. J. Catal.*, 2020, **41**, 739-755.
11. X. Yu and S. Ye, *J. Power Sources*, 2007, **172**, 145-154.

12. P. C. Okonkwo, O. O. Ige, E. M. Barhoumi, P. C. Uzoma, W. Emori, A. Benamor and A. M. Abdullah, *Int. J. Hydrog. Energy*, 2021, **46**, 15850-15865.
13. D. A. Cullen, K. C. Neyerlin, R. K. Ahluwalia, R. Mukundan, K. L. More, R. L. Borup, A. Z. Weber, D. J. Myers and A. Kusoglu, *Nat. Energy*, 2021, **6**, 462-474.
14. D. Y. Chung, S. W. Jun, G. Yoon, S. G. Kwon, D. Y. Shin, P. Seo, J. M. Yoo, H. Shin, Y.-H. Chung, H. Kim, B. S. Mun, K.-S. Lee, N.-S. Lee, S. J. Yoo, D.-H. Lim, K. Kang, Y.-E. Sung and T. Hyeon, *J. Am. Chem. Soc.*, 2015, **137**, 15478-15485.
15. T. Y. Yoo, J. M. Yoo, A. K. Sinha, M. S. Bootharaju, E. Jung, H. S. Lee, B.-H. Lee, J. Kim, W. H. Antink, Y. M. Kim, J. Lee, E. Lee, D. W. Lee, S.-P. Cho, S. J. Yoo, Y.-E. Sung and T. Hyeon, *J. Am. Chem. Soc.*, 2020, **142**, 14190-14200.
16. Z. Zhao, Z. Liu, A. Zhang, X. Yan, W. Xue, B. Peng, H. L. Xin, X. Pan, X. Duan and Y. Huang, *Nat. Nanotechnol.*, 2022, **17**, 968-975.
17. Y. Zhu, J. Peng, X. Zhu, L. Bu, Q. Shao, C.-W. Pao, Z. Hu, Y. Li, J. Wu and X. Huang, *Nano Lett.*, 2021, **21**, 6625-6632.
18. J. Wu, J. Zhang, Z. Peng, S. Yang, F. T. Wagner and H. Yang, *J. Am. Chem. Soc.*, 2010, **132**, 4984-4985.
19. C. Chen, Y. Kang, Z. Huo, Z. Zhu, W. Huang, H. L. Xin, J. D. Snyder, D. Li, J. A. Herron, M. Mavrikakis, M. Chi, K. L. More, Y. Li, N. M. Markovic, G. A. Somorjai, P. Yang and V. R. Stamenkovic, *Science*, 2014, **343**, 1339-1343.
20. H. Y. Kim, M. Jun, S. H. Joo and K. Lee, *ACS Nanosci. Au*, 2022, DOI: https://doi.org/10.1021/acsnanoscienceau.2c00045.
21. T.-H. Yang, J. Ahn, S. Shi, P. Wang, R. Gao and D. Qin, *Chem. Rev.*, 2021, **121**, 796-833.
22. E. B. Tetteh, C. Gyan-Barimah, H.-Y. Lee, T.-H. Kang, S. Kang, S. Ringe and J.-S. Yu, *ACS Appl. Mater. Interfaces*, 2022, **14**, 25246-25256.
23. Y.-T. Pan and H. Yang, *Nano Today*, 2020, **31**, 100832.
24. Z. Xia and S. Guo, *Chem. Soc. Rev.*, 2019, **48**, 3265-3278.
25. P. Strasser, S. Koh, T. Anniyev, J. Greeley, K. More, C. Yu, Z. Liu, S. Kaya, D. Nordlund, H. Ogasawara, M. F. Toney and A. Nilsson, *Nat. Chem.*, 2010, **2**, 454-460.
26. V. Stamenkovic, B. S. Mun, K. J. Mayrhofer, P. N. Ross, N. M. Markovic, J. Rossmeisl, J. Greeley and J. K. Nørskov, *Angew. Chem.*, 2006, **118**, 2963-2967.
27. V. R. Stamenkovic, B. S. Mun, M. Arenz, K. J. Mayrhofer, C. A. Lucas, G. Wang, P. N. Ross and N. M. Markovic, *Nat. Mater.*, 2007, **6**, 241-247.
28. D. Wang, H. L. Xin, R. Hovden, H. Wang, Y. Yu, D. A. Muller, F. J. DiSalvo and H. D. Abruña, *Nat. Mater.*, 2013, **12**, 81-87.
29. S. Dai, Y. You, S. Zhang, W. Cai, M. Xu, L. Xie, R. Wu, G. W. Graham and X. Pan, *Nat. Commun.*, 2017, **8**, 1-8.
30. J. Li, S. Sharma, X. Liu, Y.-T. Pan, J. S. Spendelow, M. Chi, Y. Jia, P. Zhang, D. A. Cullen, Z. Xi, H. Lin, Z. Yin, B. Shen, M. Muzzio, C. Yu, Y. S. Kim, A. A. Peterson, K. L. More, H. Zhu and S. Sun, *Joule*, 2019, **3**, 124-135.
31. H. L. Xin, S. Alayoglu, R. Tao, A. Genc, C.-M. Wang, L. Kovarik, E. A. Stach, L.-W. Wang, M. Salmeron, G. A. Somorjai and H. Zheng, *Nano Lett.*, 2014, **14**, 3203-3207.
32. M. Chi, C. Wang, Y. Lei, G. Wang, D. Li, K. L. More, A. Lupini, L. F. Allard, N. M. Markovic and V. R. Stamenkovic, *Nat. Commun.*, 2015, **6**, 1-9.

33. H. Cheng, R. Gui, H. Yu, C. Wang, S. Liu, H. Liu, T. Zhou, N. Zhang, X. Zheng, W. Chu, Y. Lin, H. Wu, C. Wu and Y. Xie, *Proc. Natl. Acad. Sci. U. S. A.*, 2021, **118**, e2104026118.
34. S. Lee, J.-H. Jang, I. Jang, D. Choi, K.-S. Lee, D. Ahn, Y. S. Kang, H.-Y. Park and S. J. Yoo, *J. Catal.*, 2019, **379**, 112-120.
35. G. Tritsaris, J. Greeley, J. Rossmeisl and J. K. Nørskov, *Catal. Lett.*, 2011, **141**, 909-913.
36. D. J. S. Sandbeck, N. M. Secher, F. D. Speck, J. E. Sørensen, J. Kibsgaard, I. Chorkendorff and S. Cherevko, *ACS Catal.*, 2020, **10**, 6281-6290.
37. The fuel cell technologies office multi-year research, development, and demonstration plan, DOI: https://www.energy.gov/sites/prod/files/2014/12/f19/fcto_myrdd_full_document.pdf).
38. S. Stariha, N. Macauley, B. T. Sneed, D. Langlois, K. L. More, R. Mukundan and R. L. Borup, *J. Electrochem. Soc.*, 2018, **165**, F492-F501.
39. L. Chong, J. Wen, J. Kubal, F. G. Sen, J. Zou, J. Greeley, M. Chan, H. Barkholtz, W. Ding and D.-J. Liu, *Science*, 2018, **362**, 1276-1281.
40. T. Yoshida and K. Kojima, *Electrochem. Soc. Interface*, 2015, **24**, 45-49.
41. E. Antolini, *Appl. Catal., B*, 2017, **217**, 201-213.
42. S. Furukawa and T. Komatsu, *ACS Catal.*, 2017, **7**, 735-765.
43. M. Luo, Y. Sun, L. Wang and S. Guo, *Adv. Energy Mater.*, 2017, **7**, 1602073.
44. Y. Yan, J. S. Du, K. D. Gilroy, D. Yang, Y. Xia and H. Zhang, *Adv. Mater.*, 2017, **29**, 1605997.
45. J. Li and S. Sun, *Acc. Chem. Res.*, 2019, **52**, 2015-2025.
46. L. Rößner and M. Armbrüster, *ACS Catal.*, 2019, **9**, 2018-2062.
47. H. Y. Kim and S. H. Joo, *J. Mater. Chem. A*, 2020, **8**, 8195-8217.
48. J. Zhang, L. Shen, Y. Jiang and S. Sun, *Nanoscale*, 2020, **12**, 19557-19581.
49. X. Li, J. Zhao and D. Su, *Small Struct.*, 2021, **2**, 2100011.
50. Y. Yuan, Z. Yang, W. Lai, L. Gao, M. Li, J. Zhang and H. Huang, *Chem.-Eur. J.*, 2021, **27**, 16564-16580.
51. J. Bai, L. Yang, Z. Jin, J. Ge and W. Xing, *Chin. J. Catal.*, 2022, **43**, 1444-1458.
52. X. Liu, J. Liang and Q. Li, *Chin. J. Catal.*, 2023, **45**, 17-26.
53. H. Chen, J. Liu, X. Wu, C. Ye, J. Zhang, J. L. Luo and X. Z. Fu, *Small*, 2022, **18**, 2204100.
54. D. Kim, J. E. Saal, L. Zhou, S. Shang, Y. Du and Z.-K. Liu, *CALPHAD: Comput. Coupling Phase Diagrams Thermochem.*, 2011, **35**, 323-330.
55. S. Wang, W. Xu, Y. Zhu, Q. Luo, C. Zhang, S. Tang and Y. Du, *ACS Appl. Mater. Interfaces*, 2021, **13**, 827-835.
56. B. Shen, L. Huang, J. Shen, K. He, C. Y. Zheng, V. P. Dravid, C. Wolverton and C. A. Mirkin, *Proc. Natl. Acad. Sci. U. S. A.*, 2021, **118**, e2105722118.
57. Z. Wang, X. Yao, Y. Kang, L. Miao, D. Xia and L. Gan, *Adv. Funct. Mater.*, 2019, **29**, 1902987.
58. K. H. J. Buschow, P. G. van Engen and R. Jongebreur, *J. Magn. Magn. Mater.*, 1983, **38**, 1-22.
59. Y. Ma, A. N. Kuhn, W. Gao, T. Al-Zoubi, H. Du, X. Pan and H. Yang, *Nano Energy*, 2021, **79**, 105465.

60. J. D. Lee, D. Jishkariani, Y. Zhao, S. Najmr, D. Rosen, J. M. Kikkawa, E. A. Stach and C. B. Murray, *ACS Appl. Mater. Interfaces*, 2019, **11**, 26789-26797.
61. Y. Xiong, Y. Yang, H. Joress, E. Padgett, U. Gupta, V. Yarlagadda, D. N. Agyeman-Budu, X. Huang, T. E. Moylan, R. Zeng, A. Kongkanand, F. A. Escobedo, J. D. Brock, F. J. DiSalvo, D. A. Muller and H. D. Abruña, *Proc. Natl. Acad. Sci. U. S. A.*, 2019, **116**, 1974-1983.
62. Y. Liao, Y. Wang, J. Liu, Y. Tang, C. Wu and Y. Chen, *Ind. Eng. Chem. Res.*, 2021, **60**, 14728-14736.
63. F. Li, Y. Zong, Y. Ma, M. Wang, W. Shang, P. Tao, C. Song, T. Deng, H. Zhu and J. Wu, *ACS Nano*, 2021, **15**, 5284-5293.
64. X. Li, Y. He, S. Cheng, B. Li, Y. Zeng, Z. Xie, Q. Meng, L. Ma, K. Kisslinger, X. Tong, S. Hwang, S. Yao, C. Li, Z. Qiao, C. Shan, Y. Zhu, J. Xie, G. Wang, G. Wu and D. Su, *Adv. Mater.*, 2021, **33**, 2106371.
65. X. Li, S. Cheng, Y. He, L. Qian, D. Zakharov, G. Wu, C. Shan, L. Zhang and D. Su, *Nano Res.*, 2022, DOI: https://doi.org/10.1007/s12274-022-5012-0.
66. Y.-T. Pan, Y. Yan, Y.-T. Shao, J.-M. Zuo and H. Yang, *Nano Lett.*, 2016, **16**, 6599-6603.
67. J. Wu, W. Gao, J. Wen, D. J. Miller, P. Lu, J.-M. Zuo and H. Yang, *Nano Lett.*, 2015, **15**, 2711-2715.
68. J. Wu, H. Shan, W. Chen, X. Gu, P. Tao, C. Song, W. Shang and T. Deng, *Adv. Mater.*, 2016, **28**, 9686-9712.
69. K. Wang, L. Wang, Z. Yao, L. Zhang, L. Zhang, X. Yang, Y. Li, Y.-G. Wang, Y. Li and F. Yang, *Sci. Adv.*, 2022, **8**, eabo4599.
70. K. Aso, H. Kobayashi, S. Yoshimaru, X. Q. Tran, M. Yamauchi, S. Matsumura and Y. Oshima, *Nanoscale*, 2022, **14**, 9842-9848.
71. T. Kaito, H. Tanaka, H. Mitsumoto, S. Sugawara, K. Shinohara, H. Ariga, H. Uehara, S. Takakusagi and K. Asakura, *J. Phys. Chem. C*, 2016, **120**, 11519-11527.
72. W.-J. Zeng, C. Wang, Q.-Q. Yan, P. Yin, L. Tong and H.-W. Liang, *Nat. Commun.*, 2022, **13**, 7654.
73. H. Liao, A. Fisher and Z. Xu, *Small*, 2015, **11**, 3221-3246.
74. S. Prabhudev, M. Bugnet, C. Bock and G. A. Botton, *ACS Nano*, 2013, **7**, 6103-6110.
75. L. G. Cesar, C. Yang, Z. Lu, Y. Ren, G. Zhang and J. T. Miller, *ACS Catal.*, 2019, **9**, 5231-5244.
76. Y. Hu, X. Guo, T. Shen, Y. Zhu and D. Wang, *ACS Catal.*, 2022, **12**, 5380-5387.
77. L. Chen, J. Zhu, C. Xuan, W. Xiao, K. Xia, W. Xia, C. Lai, H. L. Xin and D. Wang, *J. Mater. Chem. A*, 2018, **6**, 5848-5855.
78. W. Zhao, B. Chi, L. Liang, P. Yang, W. Zhang, X. Ge, L. Wang, Z. Cui and S. Liao, *ACS Catal.*, 2022, **12**, 7571-7578.
79. C. Li, W. Zhao, X. Lu, Z. Chen, B. Han, X. Zhang, J. Chen, Y. Shao, J. Huo, Y. Zhu, Y. Deng, S. Sun and S. Liao, *J. Energy Chem.*, 2023, **78**, 340-349.
80. J. Liang, N. Li, Z. Zhao, L. Ma, X. Wang, S. Li, X. Liu, T. Wang, Y. Du, G. Lu, J. Han, Y. Huang, D. Su and Q. Li, *Angew. Chem. Int. Ed.*, 2019, **58**, 15471-15477.
81. L. Zhang, X. Ji, X. Wang, Y. Fu, H. Zhu and T. X. Liu, *J. Electrochem. Soc.*, 2020, **167**, 024507.

82. Y. Jin, G. Ren, Y. Feng, S. Geng, L. Li, X. Zhu, J. Guo, Q. Shao, Y. Xu, X. Huang and J. Lu, *Nano Res.*, 2022, **15**, 9631-9638.
83. Y. Cui, Y. Wu, Z. Wang, X. Yao, Y. Wei, Y. Kang, H. Du, J. Li and L. J. J. o. T. E. S. Gan, *J. Electrochem. Soc.*, 2020, **167**, 064520.
84. W.-J. Zeng, L. Tong, J. Liu and H.-W. Liang, *J. Electroanal. Chem.*, 2022, **922**, 116728.
85. T.-W. Song, L.-J. Zuo, M. Zuo and H.-W. Liang, *J. Catal.*, 2023, DOI: https://doi.org/10.1016/j.jcat.2023.01.026.
86. W. Xu, Z. Zhu, Y. Wang, P. Cui, L. Tong, K. Zhao, J. Yuan, Z.-Y. Zhou, H.-W. Liang, N. Tian and S.-G. Sun, *J. Mater. Chem. A*, 2023, DOI: 10.1039/D2TA07784A.
87. S. Hu and W.-X. Li, *Science*, 2021, **374**, 1360-1365.
88. M. Wang, M. Wang, L. Guo, Y. Li, S. Chen and Z. Wei, *Int. J. Hydrogen Energy*, 2022, **47**, 27116-27123.
89. S.-L. Xu, S.-C. Shen, S. Zhao, Y.-W. Ding, S.-Q. Chu, P. Chen, Y. Lin and H.-W. Liang, *Chem. Sci.*, 2020, **11**, 7933-7939.
90. C.-L. Yang, L.-N. Wang, P. Yin, J. Liu, M.-X. Chen, Q.-Q. Yan, Z.-S. Wang, S.-L. Xu, S.-Q. Chu, C. Cui, H. Ju, J. Z. Zhu, Y. L. Lin, J. Shui and H.-W. Liang, *Science*, 2021, **374**, 459-464.
91. T.-W. Song, C. Xu, Z.-T. Sheng, H.-K. Yan, L. Tong, J. Liu, W.-J. Zeng, L.-J. Zuo, P. Yin, M. Zuo, S.-Q. Chu, P. Chen and H.-W. Liang, *Nat. Commun.*, 2022, **13**, 1-11.
92. Y. Zhao, C. Wang, J. Liu and F. Wang, *Nanoscale*, 2018, **10**, 9038-9043.
93. M. Chen, S. Zhou, W. Liao, Z. Wang, J. Long, Q. Zhou and Q. Wang, *ChemElectroChem*, 2022, **9**, e202200803
94. W. Zhao, Y. Ye, W. Jiang, J. Li, H. Tang, J. Hu, L. Du, Z. Cui and S. Liao, *J. Mater. Chem. A*, 2020, **8**, 15822-15828.
95. H. Zhong, H. Wu, Y. Pan, H. Li, Y. Peng, D. Banham and J. Zeng, *Int. J. Hydrogen Energy*, 2022, **47**, 40952-40960.
96. Y. Liao, L. Peng, C. Wu, Y. Yan, H. Xie, Y. Chen and Y. Wang, *Nano Res.*, 2023, DOI: 10.1007/s12274-023-5399-2.
97. M. Xie, Z. Lyu, R. Chen, M. Shen, Z. Cao and Y. Xia, *J. Am. Chem. Soc.*, 2021, **143**, 8509-8518.
98. R. Toyama, S. Kawachi, J.-i. Yamaura, T. Fujita, Y. Murakami, H. Hosono and Y. Majima, *Nanoscale Adv.*, 2022, **4**, 5270-5280.
99. H. Y. Kim, J. M. Kim, Y. Ha, J. Woo, A. Byun, T. J. Shin, K. H. Park, H. Y. Jeong, H. Kim, J. Y. Kim and S. H. Joo, *ACS Catal.*, 2019, **9**, 11242-11254.
100. Y. Cai, P. Gao, F. Wang and H. Zhu, *Electrochim. Acta*, 2017, **245**, 924-933.
101. W. Yang, L. Zou, Q. Huang, Z. Zou, Y. Hu and H. Yang, *J. Electrochem. Soc.*, 2017, **164**, H331-H337.
102. Y. Xiong, L. Xiao, Y. Yang, F. J. DiSalvo and H. D. Abruña, *Chem. Mater.*, 2018, **30**, 1532-1539.
103. T. He, W. Wang, X. Yang, F. Shi, Z. Ye, Y. Zheng, F. Li, J. Wu, Y. Yin and M. Jin, *ACS Nano*, 2021, **15**, 7348-7356.
104. Q. Cheng, S. Yang, C. Fu, L. Zou, Z. Zou, Z. Jiang, J. Zhang and H. Yang, *Energy Environ. Sci.*, 2022, **15**, 278-286.

105. Y.-H. Wen, L.-H. Zhang, J.-B. Wang and R. Huang, *J. Alloys Compd.*, 2019, **776**, 629-635.
106. W. Liu, S. Di, F. Wang and H. Zhu, *Int. J. Hydrogen Energy*, 2022, **47**, 6312-6322.
107. D. J. Rosen, A. C. Foucher, J. D. Lee, S. Yang, E. Marino, E. A. Stach and C. B. Murray, *ACS Mater. Lett.*, 2022, **4**, 823-830.
108. H. You, S. Yang, B. Ding and H. Yang, *Chem. Soc. Rev.*, 2013, **42**, 2880-2904.
109. Y. Xiong, Y. Yang, F. J. DiSalvo and H. D. Abruña, *ACS Nano*, 2020, **14**, 13069-13080.
110. X. X. Wang, S. Hwang, Y.-T. Pan, K. Chen, Y. He, S. Karakalos, H. Zhang, J. S. Spendelow, D. Su and G. Wu, *Nano Lett.*, 2018, **18**, 4163-4171.
111. K. A. Kuttiyiel, S. Kattel, S. Cheng, J. H. Lee, L. Wu, Y. Zhu, G.-G. Park, P. Liu, K. Sasaki, J. G. Chen and R. R. Adzic, *ACS Appl. Energy Mater.*, 2018, **1**, 3771-3777.
112. X.-F. Han, N. Batool, W.-T. Wang, H.-T. Teng, L. Zhang, R. Yang and J.-H. Tian, *ACS Appl. Mater. Interfaces*, 2021, **13**, 37133-37141.
113. M. Liu, A. Hu, Y. Ma, G. Wang, L. Zou, X. Chen and H. Yang, *J. Electroanal. Chem.*, 2020, **871**, 114267.
114. W. H. Lai, B. W. Zhang, Z. Hu, X. M. Qu, Y. X. Jiang, Y. X. Wang, J. Z. Wang, H. K. Liu and S. L. Chou, *Adv. Funct. Mater.*, 2019, **29**, 1807340.
115. L. Pavko, M. Gatalo, G. Križan, J. Križan, K. Ehelebe, F. Ruiz-Zepeda, M. Šala, G. Dražić, M. Geuß, P. Kaiser, M. Bele, M. Kostelec, T. Đukić, N. Van de Velde, I. Jerman, S. Cherevko, N. Hodnik, B. Genorio and M. Gaberšček, *ACS Appl. Energy Mater.*, 2021, **4**, 13819-13829.
116. M. Vondrova, C. M. Burgess and A. B. Bocarsly, *Chem. Mater.*, 2007, **19**, 2203-2212.
117. J. Li, S. Sharma, K. Wei, Z. Chen, D. Morris, H. Lin, C. Zeng, M. Chi, Z. Yin, M. Muzzio, M. Shen, P. Zhang, A. A. Peterson and S. Sun, *J. Am. Chem. Soc.*, 2020, **142**, 19209-19216.
118. V. R. Stamenkovic, B. Fowler, B. S. Mun, G. Wang, P. N. Ross, C. A. Lucas and N. M. Markovic, *Science*, 2007, **315**, 493-497.
119. X. Huang, Z. Zhao, L. Cao, Y. Chen, E. Zhu, Z. Lin, M. Li, A. Yan, A. Zettl, Y. M. Wang, X. Duan, T. Mueller and Y. Huang, *Science*, 2015, **348**, 1230-1234.
120. R. Huang, G.-F. Shao, Y. Zhang and Y.-H. Wen, *ACS Appl. Mater. Interfaces*, 2017, **9**, 12486-12493.
121. Y.-H. Wen and R. Huang, *J. Phys. Chem. C*, 2019, **123**, 12007-12014.
122. Y.-T. Pan, D. Li, S. Sharma, C. Wang, M. J. Zachman, E. C. Wegener, A. J. Kropf, Y. S. Kim, D. J. Myers, A. A. Peterson, D. A. Cullen and J. S. Spendelow, *Chem Catal.*, 2022, **2**, 3559-3572.
123. W. S. Jung, W. H. Lee, H.-S. Oh and B. N. Popov, *J. Mater. Chem. A*, 2020, **8**, 19833-19842.
124. L. Chen, J. Zhu, J. Wang, W. Xiao, W. Lei, T. Zhao, T. Huang, Y. Zhu and D. Wang, *Electrochim. Acta*, 2018, **283**, 1253-1260.
125. Z. Qiao, C. Wang, C. Li, Y. Zeng, S. Hwang, B. Li, S. Karakalos, J. Park, A. J. Kropf, E. C. Wegener, Q. Gong, H. Xu, G. Wang, D. J. Myers, J. Xie, J. S. Spendelow and G. Wu, *Energy Environ. Sci.*, 2021, **14**, 4948-4960.

126. L.-C. Lin, C.-H. Kuo, Y.-H. Hsu, L.-C. Hsu, H.-Y. Chen, J.-L. Chen and Y.-T. Pan, *Appl. Catal., B*, 2022, **317**, 121767.
127. P. Ren, P. Pei, Y. Li, Z. Wu, D. Chen and S. Huang, *Prog. Energy Combust. Sci.*, 2020, **80**, 100859.
128. Q. Gong, H. Zhang, H. Yu, S. Jeon, Y. Ren, Z. Yang, C.-J. Sun, E. A. Stach, A. C. Foucher, Y. Yu, M. Smart, G. M. Filippelli, D. A. Cullen, P. Liu and J. Xie, *Matter*, 2023, DOI: https://doi.org/10.1016/j.matt.2022.12.011.
129. Y. Zhao, J. Liu, Y. Zhao, F. Wang and Y. Song, *J. Mater. Chem. A*, 2015, **3**, 20086-20091.
130. J. Gao, X. Zhou, Y. Wang, Y. Chen, Z. Xu, Y. Qiu, Q. Yuan, X. Lin and H. J. Qiu, *Small*, 2022, **18**, 2202071.
131. P. Guo, Y. Xia, B. Liu, M. Ma, L. Shen, Y. Dai, Z. Zhang, Z. Zhao, Y. Zhang, L. Zhao and Z. Wang, *ACS Appl. Mater. Interfaces*, 2022, **14**, 53819-53827.
132. T. Ellaby, A. Varambhia, X. Luo, L. Briquet, M. Sarwar, D. Ozkaya, D. Thompsett, P. D. Nellist and C.-K. Skylaris, *Phys. Chem. Chem. Phys.*, 2020, **22**, 24784-24795.
133. L. Zhang, X. Wang and H. Zhu, *Prog. Nat. Sci.: Mater. Int.*, 2020, **30**, 890-895.
134. X. Song, L. Huang, W. He, C. Liu, F. Hu, Y. Jiang, Z. Sun and S. Wei, *J. Phys. Chem. C*, 2019, **123**, 10907-10916.
135. T. Komatsu and A. Tamura, *J. Catal.*, 2008, **258**, 306-314.
136. H. Li, X. Yu, S.-T. Tu, J. Yan and Z. Wang, *Appl. Catal., A*, 2010, **387**, 215-223.
137. X. Yu, H. Li, S.-T. Tu, J. Yan and Z. Wang, *Int. J. Hydrogen Energy*, 2011, **36**, 3778-3788.
138. S. Furukawa, K. Ehara and T. Komatsu, *Catal. Sci. Technol.*, 2016, **6**, 1642-1650.
139. S. A. Davari, S. Hu and D. Mukherjee, *Talanta*, 2017, **164**, 330-340.
140. H. Yano, I. Arima, M. Watanabe, A. Iiyama and H. Uchida, *J. Electrochem. Soc.*, 2017, **164**, F966-F972.
141. Y. Yu, H. L. Xin, R. Hovden, D. Wang, E. D. Rus, J. A. Mundy, D. A. Muller and H. D. Abruña, *Nano Lett.*, 2012, **12**, 4417-4423.

Author biographies

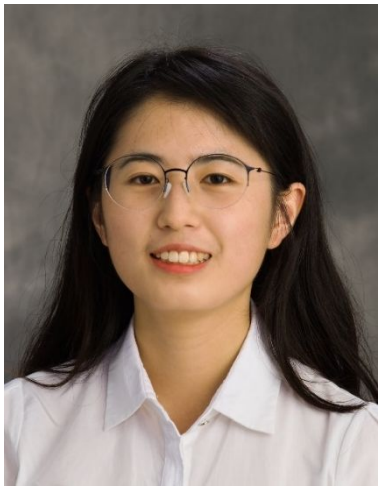

Siying Yu received her B.Sc. degree in Chemistry from Peking University in 2019. She then joined Professor Hong Yang's group at the University of Illinois at Urbana−Champaign (UIUC) as a Ph.D. student in the same year. Her graduate research has focused on the development and characterization of low-PGM electrocatalysts for fuel cell applications, non-precious metal catalysts for water electrolysis and thermal catalysis.

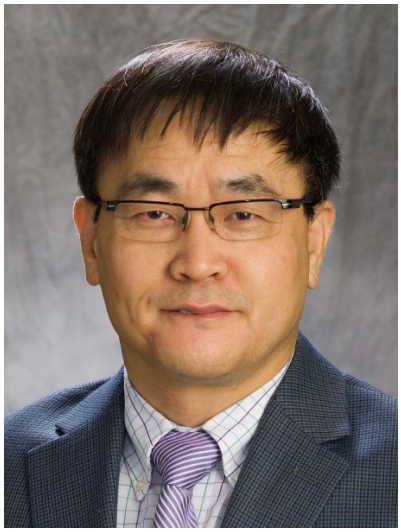

Hong Yang is the Richard C. Alkire Chair Professor in Chemical Engineering at UIUC. He received his Ph.D. degree in 1998 from University of Toronto and did his postdoctoral training as an NSERC Postdoctoral Fellow at Harvard University. He worked at University of Rochester between 2001 and 2011 and moved to UIUC in 2012. He is an elected Fellow of AAAS, the winner of the Doctoral Prize from NSERC Canada, and the recipient of the

CAREER Award from US NSF. His current research interests are on the material chemistry approach to the development of nanostructures for catalysis, energy, and sustainability applications.